



# HHS Public Access

Author manuscript

*Nat Neurosci.* Author manuscript; available in PMC 2015 December 01.

Published in final edited form as:

*Nat Neurosci.* 2015 June ; 18(6): 892–902. doi:10.1038/nn.4002.

## An acetylcholine-activated microcircuit drives temporal dynamics of cortical activity

Naiyan Chen<sup>#</sup>, Hiroki Sugihara<sup>#</sup>, and Mriganka Sur<sup>\*</sup>

Picower Institute for Learning and Memory, Department of Brain and Cognitive Sciences, Massachusetts Institute of Technology, Cambridge, MA 02139, USA.

<sup>#</sup> These authors contributed equally to this work.

### Abstract

Cholinergic modulation of cortex powerfully influences information processing and brain states, causing robust desynchronization of local field potentials and strong decorrelation of responses between neurons. Here we show that intracortical cholinergic inputs to mouse visual cortex specifically and differentially drive a defined cortical microcircuit: they facilitate somatostatin-expressing (SOM) inhibitory neurons that in turn inhibit parvalbumin-expressing inhibitory neurons and pyramidal neurons. Selective optogenetic inhibition of SOM responses blocks desynchronization and decorrelation, demonstrating that direct cholinergic activation of SOM neurons is necessary for this phenomenon. Optogenetic inhibition of vasoactive intestinal peptide-expressing neurons does not block desynchronization, despite these neurons being activated at high levels of cholinergic drive. Direct optogenetic SOM activation, independent of cholinergic modulation, is sufficient to induce desynchronization. Together, these findings demonstrate a mechanistic basis for temporal structure in cortical populations, and the crucial role of neuromodulatory drive to specific inhibitory-excitatory circuits in actively shaping the dynamics of neuronal activity.

### Introduction

Cholinergic innervation of the neocortex by afferent axons originating in the nucleus basalis (NB) of the basal forebrain<sup>1</sup> is a fundamental mechanism for modulating cortical sensory processing by influencing brain states<sup>2</sup> and the temporal dynamics of neurons<sup>3</sup>. Specifically, acetylcholine (ACh) can induce a highly desynchronized state as measured by the field potential activity of neuronal populations<sup>2</sup>, accompanied by prominent firing-rate independent decorrelation between the spike activity of individual neurons<sup>3</sup>. Both

Users may view, print, copy, and download text and data-mine the content in such documents, for the purposes of academic research, subject always to the full Conditions of use:[http://www.nature.com/authors/editorial\\_policies/license.html#terms](http://www.nature.com/authors/editorial_policies/license.html#terms)

<sup>\*</sup> To whom correspondence should be addressed: msur@mit.edu Phone: 617-253-8784 Fax: 617-253-9829.

#### Author Contributions

NC and HS designed, conducted and analyzed *ex vivo* experiments. HS and NC designed, conducted and analyzed *in vivo* experiments. NC, HS and MS wrote the manuscript. MS supervised the project.

A Supplementary Methods Checklist is available.

#### Competing financial interests

The authors declare no competing financial interests.

desynchronization and decorrelation<sup>4</sup> are considered to enhance information processing via redundancy reduction<sup>3</sup> in alert, active and attentive conditions<sup>5, 6</sup>, through direct engagement of cholinergic mechanisms<sup>5</sup>. ACh acts via thalamocortical and intracortical pathways<sup>7</sup>, which in turn may contribute to different neuromodulatory functions<sup>3</sup>. In particular, decorrelation has been shown to depend on local activation of intracortical pathways<sup>3</sup> while desynchronization has been linked to membrane potential fluctuations in cortical neurons<sup>8</sup> and to inhibition in cortical networks<sup>9</sup>. Earlier studies proposed a possible role for rhythmic-bursting layer 5 pyramidal neurons<sup>2</sup> in the generation of cortical synchronization by cholinergic inputs. However, recent computational and experimental studies have suggested that inhibitory neurons can drive decorrelation and sparse coding in the cortex<sup>10-12</sup> and experimental evidence indicates that inhibitory activity correlates with<sup>13</sup> and can induce<sup>14</sup> specific neuronal activity patterns.

The cellular and circuit mechanisms that underlie desynchronization and decorrelation observed during cortical cholinergic modulation remain unresolved, and several key questions remain open: Is ACh-induced desynchronization and decorrelation in the cortex driven by inhibitory neurons? If so, which subtypes of inhibitory neurons are responsible, and how do their functional interactions with each other and other cell types in the cortical circuit contribute to brain state and neuronal spike correlation changes? Previous work has demonstrated cholinergic facilitation of non fast-spiking inhibitory neurons<sup>15-17</sup> including somatostatin-expressing (SOM)<sup>17-19</sup>, vasoactive intestinal peptide-expressing (VIP)<sup>17, 20, 21</sup> and layer 1 (L1) inhibitory neurons<sup>20, 22, 23</sup>. However, when and under what conditions ACh drives these different neuron types, and the specific functional circuit and causal pathway by which ACh carries out desynchronization and decorrelation is unresolved. Here we demonstrate that SOM neurons are active at a greater dynamic ACh range than VIP and L1 neurons, and cholinergic inputs to the superficial layers of primary visual cortex (V1) act via SOM neurons (but not VIP and L1 neurons) to activate a specific inhibitory-excitatory cortical circuit that drives alterations of brain state synchrony and neuronal correlations.

## Results

### Cortical dynamics evoked by optogenetic ACh release

We stimulated ACh release in superficial V1 *in vivo* of urethane-anesthetized adult mice (see Online Methods: *In vivo* surgery) by cortical photostimulation of channelrhodopsin2 (ChR2)-expressing cholinergic axons from the basal forebrain, in ChAT-ChR2 transgenic mice (**Fig. 1a**). This induced robust desynchronization of the local field potential (LFP) in V1<sup>24</sup>, similar to that induced by electrical stimulation of the nucleus basalis<sup>25</sup> (**Fig. 1b,c**, **Supplementary Fig. 1a-e**), including post-stimulation decrease of low frequency events (<10 Hz) and increase of high frequency events (10 – 100 Hz) (**Fig. 1d**).

One of the ways ACh<sup>3</sup> and attention<sup>6</sup> have been proposed to enhance the representation of information is through decorrelation of neuronal responses, but the mechanisms underlying such decorrelation are unclear. We next examined whether activation of neocortical cholinergic axons can induce decorrelation by measuring the activity of single units with an array of multiple electrodes (**Fig. 1a**; see Online Methods: *In vivo* single unit recording and

data analysis), in response to both natural movies and gratings of random orientation (**Fig. 1e left**). We observed significant decorrelation between cortical neurons upon photostimulation (**Fig. 1e right**) at the level of single units (**Fig. 1f, Supplementary Fig. 1f,g**), as well as at the level of single pairwise correlations (**Supplementary Fig. 1h**) and experimental animals (**Fig. 1g**; see also **Supplementary Fig. 1i**).

### Concentration-specific responses in non-FS interneurons

To test the hypothesis that inhibitory neurons can drive ACh-induced desynchronization and decorrelation, we first examined the cholinergic responses of several candidate non fast-spiking (FS) inhibitory neurons known to be active during cholinergic modulation<sup>15, 16</sup>. We performed *ex vivo* whole-cell current clamp recordings from somatostatin-expressing (SOM) neurons (tdTomato positive neurons in SOM-TD mice), vasoactive intestinal peptide-expressing (VIP) neurons (in VIP-TD mice) and layer 1 (L1) inhibitory neurons (in wild type (WT) mice) (**Fig. 2a**). Indeed, ACh application evoked facilitatory responses in SOM<sup>17-19</sup> (but see<sup>20</sup>), VIP<sup>17, 20, 21</sup> and L1 neurons<sup>20, 22, 23</sup> (**Fig. 2b,c**). Interestingly, SOM neurons fired robustly to a wide range of ACh concentrations (1  $\mu$ M – 10 mM), consistent with their low threshold spiking properties (**Supplementary Fig. 2**)<sup>18</sup>, while VIP and L1 neurons depolarized at 100  $\mu$ M ACh but fired only at 10 mM ACh (**Fig. 2b**: Example responses evoked by 100  $\mu$ M ACh; **Fig. 2c**).

It is well established that specific subsets of inhibitory neurons connect to each other<sup>26, 27</sup>. We thus hypothesized that ACh can also indirectly induce inhibitory synaptic currents (IPSCs) in SOM, VIP and L1 neurons through cholinergic activation of defined inhibitory connections between these neurons. Indeed, ACh application evoked a barrage of inward currents in SOM, VIP and L1 neurons recorded in voltage clamp mode with high chloride internal solution in the presence of NBQX, an AMPA receptor antagonist (**Fig. 2d,e**). These responses were also concentration specific: ACh at 1-100  $\mu$ M induced responses in VIP and L1 neurons but minimally in SOM neurons while ACh at 10 mM induced large responses in all 3 cell types (**Fig. 2d**: Example responses evoked by 100  $\mu$ M ACh; **Fig. 2e**. See also **Supplementary Fig. 3d**). These inward currents comprised largely of summated IPSCs<sup>15</sup> as they were reduced significantly in the presence of GABA antagonists, particularly at lower ACh concentrations (1-100  $\mu$ M) (**Supplementary Fig. 3a-d**). Collectively, these findings suggest that the level of activation of SOM, VIP and L1 neurons, and the inhibitory inputs received by them, can change dynamically with different levels of cholinergic drive.

Recent work<sup>26</sup> indicates that SOM neurons avoid inhibiting one another but provide significant inhibition to all other inhibitory neurons including VIP and L1 neurons. VIP neurons, on the other hand, provide inhibition nearly exclusively to SOM neurons, albeit at a level several-fold weaker than SOM-VIP and SOM-L1 inhibition (but see<sup>28</sup>). We hypothesized that the cholinergic drive-dependent responses observed in SOM, VIP and L1 neurons were a result of ACh induced facilitation and indirect ACh activation of interneuron-specific inhibitory connections. In particular, the activation of SOM neurons could induce significant inhibition in VIP and L1 neurons to suppress the ACh-induced facilitatory responses at lower ACh concentrations (**Supplementary Fig. 4a**). To test this hypothesis, we transiently blocked the activity of SOM neurons by selectively expressing

archaerhodopsin-3 (Arch) in them via viral injection of a flexed Arch construct into V1 of SOM-Cre mice; in addition, we crossed SOM-Cre mice with GAD67-GFP mice (GAD67-GFP-SOM-Cre mice) for identifying inhibitory neurons in conjunction with Arch blockade of SOM neurons. We carried out current and voltage clamp recordings in slices with ACh application before and during green light stimulation of Arch in SOM neurons (**Fig. 2f,i,l**), from specific cell types that were also identified by their electrophysiological characteristics (**Supplementary Fig. 4b**). Stimulation of Arch in SOM neurons indeed abolished their cholinergic responses (**Fig. 2f-h**). Control recordings from SOM neurons in SOM-TD mice without Arch expression showed that green light stimulation alone did not induce any changes in ACh-evoked responses (**Supplementary Fig. 4c**).

To test the causal relationship between the ACh-induced facilitation of SOM responses and ACh-induced IPSCs in VIP and L1 neurons, we carried out voltage clamp recordings from putative VIP neurons (identified by their non fast-spiking properties, presence of GFP in GAD67-GFP-SOM-Cre mice and absence of hyperpolarization with green light stimulation; **Fig. 2i**) and from L1 neurons (GFP-negative, non SOM-expressing neurons in layer 1 of SOM-Cre mice; **Fig. 2i**) while ACh was administered at 100  $\mu$ M. Indeed, photostimulation of Arch in SOM neurons significantly reduced the ACh-induced IPSCs in both putative VIP neurons (**Fig. 2j,k**, see also **Supplementary Fig. 3e**) and L1 neurons (**Fig. 2m,n**, see also **Supplementary Fig. 3f**). Thus, these data support the hypothesis that defined inhibitory connections between molecularly distinct, non-FS inhibitory subtypes and their intrinsic firing properties can shape their responses at different levels of cholinergic drive (**Supplementary Fig. 4a**).

### ACh directly facilitates SOM neurons

We next investigated the role of SOM neurons in the densely-connected microcircuit of SOM, parvalbumin-expressing (PV) inhibitory neurons and pyramidal (PYR) neurons<sup>26</sup> during cholinergic modulation using both *ex vivo* current and voltage whole-cell patch clamp recordings (**Supplementary Fig. 5a**). For SOM neurons (in SOM-TD mice; **Supplementary Fig. 5b**), ACh evoked robust depolarization which persisted in the presence of glutamatergic and GABAergic antagonists (**Fig. 3a,b**), indicating that it was due to direct action of ACh. This response was prolonged and peaked within 10s (**Supplementary Fig. 5c**). In addition, the response was significantly reduced in the presence of the cholinergic antagonists mecamylamine and atropine (**Supplementary Fig. 6a,b**), showing that both muscarinic and nicotinic receptors mediate this response.

In voltage clamp recordings using low chloride internal solution, we observed a barrage of inward currents (**Supplementary Fig. 5d**) which comprised NBQX-insensitive muscarinic receptor and nicotinic receptor mediated currents (**Supplementary Fig. 6c-e**). We further confirmed that both muscarinic and nicotinic receptors are expressed in SOM neurons (**Supplementary Fig. 6f**). Thus, SOM neurons are directly activated via both types of receptors.

### ACh-induced SOM-mediated IPSCs in PV neurons

Next, we characterized the cholinergic responses of PV neurons (in PV-TD mice; **Supplementary Fig. 5f**). ACh did not evoke any excitatory responses when recorded in current clamp<sup>15</sup> (**Supplementary Fig. 5g**) and voltage clamp mode with low chloride internal solution (**Supplementary Fig. 5h**) but induced IPSCs when recorded in voltage clamp mode with high chloride internal solution in the presence of NBQX (**Supplementary Fig. 5i, Supplementary Fig. 7a**). Thus, the ACh-induced responses in PV neurons require GABAergic transmission.

We hypothesized that the IPSCs in PV neurons were due to activation of SOM neurons by ACh and subsequent inhibitory drive from SOM to PV neurons (**Fig. 3a inset**). To test this hypothesis, we carried out voltage clamp recordings of IPSCs from putative PV neurons (identified by their fast-spiking properties and presence of GFP in GAD67-GFP-SOM-Cre mice) in slices containing Arch-expressing SOM neurons (**Fig. 3c, Supplementary Fig. 4b**). Indeed, photostimulation of Arch in SOM neurons reduced the ACh-induced increase in IPSCs in the putative PV neurons (**Fig. 3d-e, see also Supplementary Fig. 7c**), suggesting that ACh-induced facilitation of SOM responses can induce IPSCs in PV neurons.

### ACh-induced SOM-mediated IPSCs in PYR neurons

Next, we investigated if ACh-induced facilitation of SOM responses could induce IPSCs in PYR neurons. PYR neurons were identified as GFP-negative neurons in GAD67-GFP mice (**Supplementary Fig. 5j**) and recorded in voltage clamp mode with high chloride internal solution in the presence of NBQX. ACh induced a barrage of IPSCs (**Supplementary Fig. 5m**) that also required GABAergic transmission (**Supplementary Fig. 7b**). To test the hypothesis if cholinergic activation of SOM neurons contribute to the IPSCs in PYR neurons (**Fig. 3a inset**), we selectively recorded IPSCs from putative PYR neurons (identified by their pyramidal morphology and absence of GFP in SOM-Cre mice) in slices containing Arch-expressing SOM neurons (**Fig. 3f, Supplementary Fig. 4b**). Similar to PV neurons, photostimulation of Arch in SOM neurons reduced the ACh-induced increase in IPSCs in the putative PYR neurons (**Fig. 3g,h, see also Supplementary Fig. 7d**). Thus, these data reveal the circuit interactions between SOM, PV and PYR neurons in the context of ACh modulation: SOM neurons are directly activated by ACh, and release GABA to evoke IPSCs in PV and PYR neurons (**Fig. 3a inset**).

Previous work has shown that cholinergic agonists can inhibit GABA release from PV neurons<sup>29</sup>. Because PV neurons widely inhibit PYR neurons<sup>26, 30</sup>, reduced GABA release from PV neurons can disinhibit PYR neurons<sup>29</sup> to facilitate excitatory synaptic events<sup>31</sup>. It is thus possible that disinhibition of PYR neurons can occur via SOM-mediated PV inhibition. To investigate this mechanism, we recorded ACh induced responses in low chloride solution (**Supplementary Fig. 5l**). Indeed, ACh induced a barrage of inward currents that were significantly reduced by NBQX (**Supplementary Fig. 8a-c**), consistent with this response comprising summated excitatory synaptic events<sup>32</sup>. These excitatory currents were also reduced by GABA antagonist (**Supplementary Fig. 8d-f**), supporting the presence of inhibitory neuron-mediated disinhibition. The prolonged component of this response however remained in the presence of glutamatergic or GABAergic antagonists

(**Supplementary Fig. 8b,e**), suggesting possible roles of intrinsic cholinergic mechanisms<sup>33, 34</sup>.

To further investigate the role of SOM neurons in mediating possible transient PYR neuronal disinhibition, we performed recordings of these inward currents in slices containing Arch-expressing SOM neurons. Indeed, photostimulation of Arch in SOM neurons also transiently blocked the ACh-induced excitatory currents in PYR neurons (**Supplementary Fig. 8g-i**). Likewise, the prolonged component was not abolished by SOM hyperpolarization (**Supplementary Fig. 8h**). These data collectively suggest the presence of a circuit comprising multiple pathways that can powerfully modulate PYR neuronal responses: direct inhibition by SOM neurons on PYR neurons, indirect disinhibition via PV on PYR neurons and an intrinsic response. These pathways may together induce the diverse sub-threshold hyperpolarizing and depolarizing responses<sup>32</sup> revealed in current clamp recordings of single PYR neurons (**Supplementary Fig. 5k**), leading to insignificant change in firing at the population level *in vivo* (see below).

### ACh evokes specific responses in SOM, PV and PYR neurons

Our findings above highlight the role of cholinergic-activated SOM neurons acting as a powerful hub of inhibition to modulate principal neurons in the cortex, thereby making it a strong candidate to mediate ACh-induced temporal changes in neuronal activity. Before probing the possible causal link between the SOM-driven microcircuit and LFP desynchronization/ neuronal decorrelation, we first examined whether cholinergic responses *in vivo* were consistent with that observed *ex vivo*. We performed *in vivo* targeted cell-attached recordings from identified RFP-labeled SOM neurons (labeled with viral injection of a floxed RFP construct in V1 of ChAT-ChR2 mice crossed with SOM-Cre mice, **Fig 4a**) and PV neurons (similarly labeled in ChAT-ChR2-PV-Cre mice, **Fig 4d**), as well as *in vivo* recording of putative PYR neuron single units (in ChAT-ChR2 mice, **Fig. 4g**) within the superficial layers of V1. Neuron types were also distinguished by their spike shape (**Supplementary Fig. 9**). Indeed, cholinergic responses induced by activation of ChAT-ChR2 axons *in vivo* agreed with that observed *ex vivo*. Robust facilitatory responses were observed in SOM neurons (**Fig. 4b,c**) while suppressive responses were observed in PV neurons (**Fig. 4e,f**). In putative PYR neurons, however, there was no significant change in response rate (**Fig. 4h,i**). Thus, endogenous ACh release via photostimulation evokes distinct *in vivo* signatures from SOM, PV and PYR neurons: SOM neurons are facilitated, PV neurons are suppressed, and the mean spike rate of PYR neurons does not change but their visual responses are decorrelated.

### ACh-induced cortical dynamics is mediated by SOM neurons

We next examined whether SOM neurons can mediate the ACh-induced changes in temporal dynamics of cortical activity, including LFP desynchronization and neuronal decorrelation (Fig.1). To establish a causal relationship between these phenomena and SOM neurons, we expressed Arch in SOM neurons by viral injection in ChAT-ChR2-SOM-Cre mice (**Fig. 5a**). Blue light induced ChAT-ChR2 stimulation facilitated SOM neurons, but green light activation of Arch simultaneously with blue light stimulation of ACh release blocked the facilitation and even reduced responses below background, consistent with



hyperpolarization of SOM neurons by Arch (**Fig. 5b,c**). The LFP in the Arch-injected V1 area was desynchronized after activation of ChAT-ChR2 axons; however, this modulation was absent when Arch was activated (and SOM neurons transiently inactivated) during ChAT-ChR2 stimulation (**Fig. 5d,e**). This finding was consistent across different pre-stimulation cortical states (**Supplementary Fig. 10**). Control experiments in ChAT-ChR2 animals without Arch expression demonstrated that green light presentation was not sufficient to abolish the desynchronization (**Supplementary Fig. 11a-c**). These findings thus directly demonstrate that SOM neurons play a critical role in cholinergic-induced desynchronization of network activity in the superficial layers of V1.

To examine the effect of SOM neurons on decorrelation of neuronal activity, we carried out single-unit recordings in ChAT-ChR2-SOM-Cre mice within the region of V1 where Arch was expressed in SOM neurons (**Supplementary Fig. 12a**). ChAT-ChR2 activation with blue light induced decorrelation between neurons, but the decorrelation was blocked during green light activation of Arch (**Fig. 5f,g, Supplementary Fig. 12b**). In control ChAT-ChR2 experiments without Arch expression, green light alone did not alter the extent of decorrelation (**Supplementary Fig. 11d-f**). It is also worth mentioning that the decorrelation and its blockade by SOM hyperpolarization was observed to be firing rate independent (**Fig. 4i, Fig. 5h, Supplementary Fig. 12c**), thereby implicating distinct mechanisms from spike rate dependent correlation changes<sup>35</sup>.

Decorrelation can improve visual coding by reducing redundancy between neurons<sup>3</sup>. We carried out a simple discrimination analysis<sup>3</sup> and found that decorrelation indeed improved discrimination performance; this improvement was also blocked by activation of Arch in SOM neurons (**Supplementary Fig. 12d**). Collectively, these data demonstrate that cholinergic activation of SOM neurons drives neuronal decorrelation in the superficial layers of V1 and thus potentially contributes to enhanced information processing.

### VIP and L1 neurons do not mediate ACh-induced IPSCs

Recent work has revealed direct, weak inhibition by VIP on SOM neurons<sup>26</sup> and indirect modulation of layer 5 PYR neurons by L1 neurons via layer 2/3 inhibitory neurons<sup>27</sup>. We thus examined if these functional connections could modulate layer 2/3 PYR neurons to alter desynchronization/decorrelation during cholinergic modulation. We carried out voltage clamp recordings from PYR neurons in VIP-Cre and 5HT3a-Cre slices containing Arch-expressing VIP neurons and Arch-expressing 5HT3a-Cre positive L1 neurons (**Supplementary Fig. 13a,e**) respectively. Although the 5HT3aR-expressing interneurons are known to be heterogeneous<sup>36</sup>, we targeted the optogenetic stimulation specifically to layer 1 of visual cortex. Interestingly, hyperpolarization of VIP neurons by Arch (**Supplementary Fig. 13a,b**) did not block but instead facilitated IPSCs in PYR neurons (**Supplementary Fig. 13c,d**). On the other hand, hyperpolarization of 5HT3aR-expressing L1 neurons by Arch (**Supplementary Fig. 13e,f**) had no significant effect on IPSCs in PYR neurons (**Supplementary Fig. 13g,h**). These findings suggest that VIP but not L1 neurons can alter inhibitory transmission to layer 2/3 PYR neurons during cholinergic modulation, possibly through the VIP-SOM<sup>26</sup> connection (**Supplementary Fig. 4a**).

### VIP neurons do not mediate ACh-induced cortical dynamics

We then examined the effect of VIP neurons on cortical desynchronization in ChAT-ChR2-VIP-Cre mice where we expressed Arch specifically in VIP neurons. Hyperpolarization of VIP neurons did not have a significant effect on ChAT-ChR2 induced cortical desynchronization (**Fig. 6a-c**). This was also observed at high power of ChAT-ChR2 stimulation (**Supplementary Fig. 10**). The conclusion held for a range of pre-stimulation cortical states observed in our recordings (**Supplementary Fig. 1a-d, Supplementary Fig. 10**). Thus, under our conditions LFP desynchronization due to intracortical ACh release directly involves SOM neurons but not VIP neurons.

In the absence of cholinergic stimulation, hyperpolarizing VIP neurons can induce IPSCs in PYR neurons (**Supplementary Fig. 13i,j**). To investigate if hyperpolarizing VIP neurons can change cortical synchronization independent of the cholinergic pathway, we performed green light stimulation of ChAT-VIP-Arch animals. Indeed, VIP neuronal hyperpolarization in the absence of ChAT-ChR2 stimulation was also sufficient to induce cortical desynchronization (**Fig. 6d,e**). This can likely be explained by the inactivation of VIP to SOM inhibition (**Supplementary Fig. 4a**) and consequential activation of the microcircuit comprising SOM-PYR and SOM-PV-PYR connections to induce cortical desynchronization similar to that observed with ChAT-ChR2 stimulation.

### SOM-activation is sufficient to evoke cortical dynamics

Our data reveals the important role SOM neurons play in driving ACh-induced desynchronization. A final question remains: is direct SOM activation independent of the cholinergic pathway sufficient to evoke desynchronization? To enable direct activation of SOM neurons, we selectively expressed ChR2 in SOM neurons by viral injection in SOM-Cre mice (**Fig. 7a**). Indeed, blue light stimulation of ChR2-expressing SOM neurons induced robust desynchronization of LFP in V1 (**Fig. 7b,c**), similar to that observed during cholinergic modulation. Hence, these data suggests that direct SOM activation is sufficient to induce desynchronization and further establishes the crucial role SOM neurons play in driving the temporal dynamics of cortical activity.

## Discussion

Decorrelation between neurons can enhance<sup>3</sup> and even optimize<sup>7</sup> information processing. During execution of attentional tasks, decorrelation has been demonstrated to enhance population sensitivity to stimulus changes and the signal-to-noise ratio of neural signals<sup>6</sup>. Our study provides the first demonstration of a specific subtype of inhibitory neuron that can contribute to such temporal alterations of spike trains in the context of cholinergic modulation, a major neuromodulatory pathway implicated in attention and arousal<sup>5</sup>. Specifically, we show that direct facilitation of SOM neurons at wide ranges of cholinergic drive can activate both direct inhibition and possibly indirect PV disinhibition on PYR neurons. The activation of this microcircuit can consequently drive a firing-rate independent decorrelation of PYR neuronal spike trains.



We further demonstrate that VIP and L1 neurons can also be facilitated by ACh, albeit effectively only at higher ACh concentration ranges due to inhibition by SOM neurons<sup>26</sup>. This finding is supported by previous work that has demonstrated stronger SOM-VIP and SOM-L1 than VIP-SOM connections<sup>26</sup> and is perhaps facilitated by the uniquely low threshold firing properties of SOM neurons (Supplementary Fig. 2)<sup>18</sup>. Although our findings (Fig. 2c, Supplementary Fig. 1e) support previous observations that cholinergic modulation of VIP neurons and cortical desynchronization is correlated with cholinergic drive<sup>20</sup>, we did not observe any reduction of cholinergic-driven cortical desynchronization when VIP neurons were hyperpolarized. Instead, VIP hyperpolarization alone could induce cortical desynchronization, possibly through the disinhibition of SOM neurons<sup>26</sup> and the consequent activation of the SOM-driven microcircuit (Fig. 6). Collectively, our data clearly demonstrate that the cholinergic activated inhibitory neuron subtypes<sup>15, 16, 18, 20-23</sup> are not all active simultaneously but at different dynamic ranges – a finding that resolves some of the complexities of ACh mechanisms. Specifically, it is not clear whether all ACh-modulated cell types are involved simultaneously in all ACh-mediated brain functions. Based on our findings, we propose instead that cholinergic activated cell types can reorganize themselves into specialized microcircuits that are engaged at different levels of cholinergic drive to mediate distinct brain functions. SOM neurons can play a crucial functional role in the active shaping of temporal structure of neural activity while VIP and L1 neurons may contribute to functions requiring higher cholinergic drive such as gain control during locomotion<sup>21</sup> or associative fear learning<sup>23</sup>.

Our results indicate that direct SOM activation via both muscarinic and nicotinic receptors by intracortical ACh is critical for the generation of network desynchronization<sup>1, 4</sup>, thereby extending previous work that has demonstrated the role of both cholinergic receptors in cholinergic desynchronization<sup>24</sup>. Our finding (Fig. 2c, Supplementary Fig. 10) also agrees with parallel observations of state-dependent SOM activation<sup>37, 38</sup> and state-dependent variation in cholinergic output in the cortex<sup>39</sup> where more awake states favor both greater ACh release and higher SOM activity. Our findings, however, do not rule out other alternative mechanisms that can underlie the generation of synchronization and desynchronization. In fact, rhythmic-bursting layer 5 pyramidal neurons<sup>2</sup>, thalamocortical pathways<sup>40</sup>, intracortical glutamatergic inputs<sup>41</sup> and direct/indirect neuromodulatory inputs<sup>2</sup> including serotonin pathways<sup>42</sup> can contribute to global changes in cortical state. Furthermore, slow oscillations originating in deeper cortical layers<sup>43</sup> can propagate<sup>44</sup> and interact with distinct cholinergic-activated cortical circuits across layers to lead to layer-specific patterns of cortical activation.

By performing local optogenetic stimulation of ChAT-ChR2 axons in the superficial layers of V1, we were able to focus on how cortical microcircuits can contribute to cholinergic desynchronization at a local scale. We have identified the SOM driven microcircuit as playing an important role in local cholinergic desynchronization; however, it is possible that other factors including intrinsic properties of PYR neurons<sup>45</sup> may also contribute to the phenomenon at a global level.

The co-existence of neuronal decorrelation and LFP desynchronization during ACh-induced SOM activation supports co-variation of temporal population activity with cortical states<sup>4</sup>

and function<sup>46</sup>. Global cortical fluctuations have been proposed to induce neuronal correlations<sup>4</sup>. During cholinergic modulation, these global fluctuations are suppressed, as reflected by a decrease in large amplitude, low frequency activity (Fig. 1d)<sup>2</sup> thereby leading to neuronal decorrelation<sup>4</sup>. Small amplitude, high frequency activity then dominates<sup>2</sup> in the decorrelated states. Previous findings have however revealed the existence of highly correlated neuronal pairs in decorrelated states<sup>10</sup>. Future work will be necessary to characterize possible cell assemblies in the ACh-induced decorrelated states.

Our data agree with previous work that has demonstrated an increase in correlation when circuit inhibition is reduced<sup>12</sup> and suggest that SOM-activated pathways can provide a source of inhibition to induce decorrelation in the local circuit. Therefore, a central question arising from this work is how the cholinergic-activated, SOM-driven neural circuit can mediate temporal changes in neural activity. It is possible that this phenomenon may share common mechanisms with that mediating surround responses of V1 neurons. ACh enhances surround suppression<sup>47</sup>, which is importantly mediated by SOM neurons<sup>37</sup>. Activation of the surround reduces spike activity but can induce decorrelation<sup>48</sup> and increase high frequency components of the LFP<sup>49</sup>. Our results bridge these observations with evidence that SOM neurons can also mediate temporal alteration of cortical activity via cholinergic modulation, thereby suggesting that ACh-evoked, top down cholinergic modulation in the temporal domain and visual stimulus evoked, bottom-up modulation in the spatial domain may share the same circuit mechanisms involving SOM neurons.

Our findings also help to reconcile seemingly contradictory effects of cholinergic modulation and nucleus basalis stimulation on V1 neurons<sup>7</sup>. Cortical cholinergic activation has been linked to both GABA-mediated suppression<sup>3, 50</sup> and facilitation of visual responses of V1 neurons<sup>7, 47, 50</sup>. These findings can in principle be explained by our results where direct cholinergic activation of SOM neurons can drive both direct inhibition and possibly indirect disinhibition<sup>19</sup> on PYR neurons to vary their firing rate according to the relative strengths of the two pathways. Our results also extend the conclusions of earlier slice studies<sup>15, 16</sup> which have demonstrated excitation of non fast-spiking inhibitory neurons and induction of an inhibitory barrage in fast-spiking and pyramidal neurons by ACh.

It is worth mentioning that mAChR-mediated facilitatory responses have also been observed in PYR neurons at a slower time scale<sup>25, 32-34</sup> than that considered in our work. These responses have been shown to be mediated by both direct actions of ACh on PYR neurons and indirect actions via cortical astrocytes to drive ACh-induced plasticity<sup>25, 33, 34</sup> (Supplementary Fig. 8b, e, h). Together with our data showing SOM neurons as a dominant driver of both decorrelation and desynchronization in cortical networks, these findings suggest that the diffuse cholinergic innervation of cortex is transformed by distinct ACh-responsive cell types and their specialized microcircuits acting across distinct time scales to enable highly specific brain functions.

## Online Methods

### Mice

*In vivo* experiments involving local field potential, single unit and cell-attached recordings were performed on adult mice between 2 - 6 months old. Slice experiments involving whole-cell patch clamp recordings were performed on P13 – P28 mice. Mice of both genders were used. These animals were housed under 12/12 hour light/dark cycle and up to 5 animals per cage. The following mouse lines were used: **Figure 1:** ChAT-ChR2-EYFP line 6 (ChAT-ChR2)<sup>51</sup>. **Figure 2 and 3:** SOM-TD and VIP-TD mice were generated by crossing the CAG-tdTomato *+/+* mice<sup>52</sup> (td, Jackson labs) with SOM-Cre knockin driver mice (SOM-Cre*+/+*, Jackson Labs) and VIP-Cre knockin driver mice (VIP-Cre*+/+*, Jackson Labs); Arch-GFP was expressed in SOM neurons by injecting the AAV8-CAG-FLEX-Arch-GFP virus (Arch, Ed Boyden lab (MIT) and UNC Vector Core)<sup>53</sup> into SOM-Cre*+/-* mice; or into GAD-67-GFP-SOMCre mice generated by first crossing GAD-67-GFP with SOM-Cre*+/+* mice; C57BL6 (WT). **Figure 4:** ChAT-ChR2; ChAT-ChR2-SOM-Cre and ChAT-ChR2-PV-Cre mice were generated by crossing ChAT-ChR2 *+/-* mice with SOM-Cre*+/+* and PV-Cre knockin driver mice (PV *+/+*, Jackson Labs) respectively<sup>54</sup>. Viral injection of the rAAV9/LS2L-dsRed-Exp virus (UNC Vector Core) containing the *loxP-STOP-loxP-RFP* construct<sup>55, 56</sup> was used to label SOM or PV neurons with RFP. **Figure 5:** Arch-GFP was expressed in SOM neurons by injecting the Arch virus into ChAT-ChR2-SOM-Cre-mice generated by crossing ChAT-ChR2 *+/-* with SOM-Cre *+/+* mice. **Figure 6:** Arch-GFP was expressed in VIP neurons by injecting the Arch virus into ChAT-ChR2-VIP-Cre-mice generated by crossing ChAT-ChR2 *+/-* with VIP-Cre *+/+* mice. **Figure 7:** ChR2 was expressed in SOM neurons by injecting the AAV1.EF1.dflox.hChR2(H134R)-mCherry.WPRE.hGH virus (Penn Vector Core) into SOMCre *+/-* mice. **Supplementary Figure 5:** SOM-TD; PV-TD mice were generated by crossing the td mice with PV-Cre*+/+*; GAD-67-GFP<sup>57</sup> or C57BL6 (WT). **Supplementary Figure 6:** RFP was expressed in SOM neurons by injecting the AAV-LS<sub>2</sub>L-RFP virus into ChAT-ChR2-SOM-Cre-mice; SOM-TD. **Supplementary Figure 13:** Arch-GFP was expressed in VIP and 5HT3aR-expressing neurons by injecting the AAV-CAG-FLEX-Arch-GFP virus (Arch) into VIP-Cre*+/-* mice and 5HT3aR-Cre knockin driver mice (5HT3aR-Cre*+/-*, Gensat); All experiments were performed under protocols approved by the Animal Care and Use Committee at MIT and conformed to NIH guidelines.

### Viral injection

The procedure was similar to that described earlier<sup>54, 55</sup>. Briefly, adult mice were anesthetized in isoflurane before the skull was thinned and the dura in primary visual cortex (V1) was punctured using a glass micropipette filled with virus. A volume of 0.25  $\mu$ l of virus was injected at the depth of 250  $\mu$ m. Experiments were performed at least 2 weeks post-injection.

***In vivo* surgery**—Mice were anesthetized with urethane (1.15 mg/g). Ophthalmic ointment was used to protect the animal's eyes during the surgery and replaced with silicon oil during imaging. Body temperature was maintained at 37.5°C with a heating pad. A metal headplate was attached to the skull with cyanoacrylate glue and dental acrylic. A 2  $\times$  2 mm

craniotomy was made over V1 which was later covered with a thin layer of 2% agarose in ACSF (140 mM NaCl, 5mM KCl, 2 mM CaCl<sub>2</sub>, 1mM MgCl<sub>2</sub>, 0.01 mM EDTA, 10 mM HEPES, 10 mM glucose, pH 7.4).

***In vivo* cell-attached recording and data analysis**—Glass pipettes (1.5 μm tip size, 3–7 MΩ) filled with Alexa dye 488 (A488, Invitrogen, Carlsbad, CA) and held at positive pressure were visually-guided into V1 with a two-photon scanning microscope (Sutter Instruments) using ScanImage software (Karel Svoboda Lab, HHMI Janelia Farm)<sup>58</sup> and directed to 100 - 200 μm below the pial surface (layer 2/3) using a micromanipulator<sup>55</sup>. Cells were imaged using a 25×, 0.95-N.A. lens (Olympus Optical) at an excitation wavelength of 910 nm. The fluorescence was detected using photomultiplier tubes (R6357; Hamamatsu). The resistance of the pipette was monitored during the penetration by delivering -0.5 nA current pulses for 6.3 ms at 0.55 Hz with Clampex software (Axon Instruments, v8.1) and Axoclamp-2A amplifier (Axon Instruments). When a seal during the advancement of pipette was obtained (assessed by increase in pipette tip resistance) and well-isolated spikes were detected on Clampex during visual stimuli presentation, sustained negative pressure was applied (0.2–0.6 psi) to secure the seal<sup>59</sup>. To fill the recorded cells, current pulses (35 ms, 900–2000 nA) were delivered at 15 Hz for 30–60 s. Recordings were performed at a sampling rate of 30 KHz and filtered between 300 Hz and 10 KHz. The pClamp data was analyzed with Clampfit software v 10.2 (MDS Analytical Technologies) for spike detection and the analyzed data was then imported in Matlab and further analyzed with custom-written scripts. In Fig. 4c, firing rates were normalized by the mean firing rate across 8s of spontaneous responses before ChAT-ChR2 stimulation. In Figs. 4f and 4i, firing rates were normalized by the mean visual responses before ChAT-ChR2 stimulation.

***In vivo* single unit recording and data analysis**—Single-unit extracellular recordings<sup>25</sup> were made using tungsten microelectrodes (0.8 MΩ; FHC). The signal was amplified and recorded using the Plexon Neurotechnology Research Systems (4-8 channels, 40 KHz at 12-bit resolution, Plexon Inc.). The signal was thresholded using an online amplitude discriminator and played over an integrated stereo amplifier (Optimus). Offline analysis to sort waveforms for each unit was performed using commercial programs (Offline Sorter version 2.8.8; Plexon Inc.).

Post processing was performed with in-house code written in MATLAB. Units were selected by two criteria for further analysis: visual responsiveness (paired t-test, P<0.05) and firing rate (>0.1 Hz). To avoid artifacts due to the same unit being picked up by more than one electrode, we removed units which had high correlation with others (pair-wise between-units correlation coefficient >0.1, with 1 KHz bin). For correlation analysis across units, we first binned responses at 100 ms (10 Hz) (See Fig. 1f, Supplementary Fig. 1g) before the mean Pearson correlation coefficient for each cell was calculated using all pairs of responses between the cell and other cells recorded simultaneously<sup>3</sup>. Population averaged correlation coefficients in Fig. 1g, 5g Supplementary Fig. 1i and 11f were computed by first averaging the correlation coefficient across all cells recorded simultaneously before taking the mean of these averaged correlation coefficients for each experiment. The single Pearson correlation coefficients between all pairs of responses are also plotted in Supplementary Fig. 1h, 12b.

The discrimination analysis in Supplementary Fig. 12d was computed as previously reported<sup>3</sup>. Responses were first binned in 100 ms segments. Discriminability was then calculated by comparing the similarity of single-trial responses to two templates comprising mean trial-averaged responses. Each discrimination was quantified by calculating the Euclidean distance between (a) single-trial responses in a given bin and the mean trial-averaged responses in the same bin, and between (b) the single-trial responses and the mean trial-averaged responses in a different bin. Discrimination was assigned correct when the distance (a) was smaller than distance (b). The discrimination performance of both control and light-stimulated experiments was normalized by the maximum performance of the control experiment for comparison. Data sets with more than 9 units were used for this analysis. Two-way ANOVA was used to assess effect of number of units included to calculate discrimination performance, and effect of light stimulation.

***In vivo* local field potential (LFP) recording and data analysis**—The LFP recordings were made using a glass pipette (2.5 – 3  $\mu\text{m}$  tip size, 2-3  $\text{M}\Omega$ ) to prevent optogenetic laser stimulation-induced artifacts<sup>60</sup>. The pipette, filled with A488 and Alexa dye 594 (A594), was visually-guided into V1 with a microscope and directed 100 - 200  $\mu\text{m}$  below the pial surface (layer 2/3) using a micromanipulator. A single channel on the Plexon Neurotechnology Research Systems was used to amplify and record the signal. The LFP signal before and during laser stimulation (1-3 sec) was analyzed using in-house code written in MATLAB to construct the power spectrum.

### Visual and optogenetic stimulation

Natural movies and random orientation gratings were displayed on a 19 inch LCD monitor situated 15 cm from the eyes. Experiments with natural stimuli consisted of 40 – 60 trials where each trial comprised a set each of control and optogenetic stimulation conditions. Each set comprised three 5-seconds natural movies (128  $\times$  128 pixels) selected from the van Hateren natural movie database. Each movie was preceded by a control period consisting of 3s of blank grey screen and 2s of still image of the first movie frame to avoid onset effects. Multiple trials were performed with alternating absence and presence of ChAT-ChR2 stimulation synchronized to the start of each movie (see Fig. 1e). Arch stimulation preceded by 1s and continued for the duration of the ChAT-ChR2 stimulation so as to ensure suppression of SOM neurons during this period.

Experiments with random orientation gratings consisted of 40 – 60 trials where each trial comprised 3 repeats of alternating 4s of blank screen and 4s of random orientation grating presentation. ChAT-ChR2 stimulation was synchronized to the start of the third repeat of grating presentation (see Fig. 1e). Arch stimulation preceded by 1s and continued for the duration of the ChAT-ChR2 stimulation. Random orientation grating stimuli were generated with the Psychophysics toolbox<sup>61</sup> in Matlab. The stimuli consisted of square wave drifting gratings at 100% contrast in 8 randomly-permuted directions, each 45 degrees apart and lasting for 450 ms.

To perform optogenetic stimulation of ChR2 and Arch, we used diode-pumped solid state blue and green lasers with analog intensity control (MBL-III-473 (Blue, 473 nm) and MBL-

III-532 (Green, 532 nm), OptoEngine, LLC). The stimulation parameters are as follows: **Blue light**: 1-5s duration, 20 Hz, 10 ms pulse width, 1 mW/mm<sup>2</sup> (used in Fig. 7), 10 mW/mm<sup>2</sup> (low ChAT-ChR2 stimulation intensity, used in all Figures except Fig. 7 and Supplementary Fig. 10 right), 30-60 mW/mm<sup>2</sup> (high ChAT-ChR2 stimulation intensity, used in Supplementary Fig. 10 right); **Green light**: 5-15s duration, continuous light, 0.1-1 mW/mm<sup>2</sup>. Pulse patterns were driven via custom D/A optogenetics software written in Matlab. The onset of visual stimuli was synchronized to the initiation of cell-attached spike, single unit, LFP recordings and optogenetic stimulation via trigger pulses. Blue laser light was focused onto superficial layers of V1 using a 10x objective lens. The estimated area is approximately 0.8 mm<sup>2</sup>.

Blue light stimulation of V1 in ChAT-ChR2<sup>62</sup> mice leads to photoactivation of cholinergic axons from the basal forebrain and a small, localized set of intrinsic cholinergic interneurons. The functional consequences of the activation of the intrinsic cholinergic interneurons have however been shown to be limited<sup>63, 64</sup>.

### Slice physiology

Coronal slices (300 µm) of visual cortex were cut in slicing buffer (< 4 °C, perfused with carbogen comprising 95% O<sub>2</sub>/5% CO<sub>2</sub>, pH 7.33 – 7.38) with a vibratome (Leica VT 1200S) and incubated in artificial cerebral spinal fluid (ACSF) at room temperature for at least 30 min before being transferred to a slice chamber for patch-recordings. All experiments were performed in carbogen-perfused ACSF. The ACSF contained (in mM): NaCl, 130; NaHCO<sub>3</sub>, 24; KCl, 3.5; NaH<sub>2</sub>PO<sub>4</sub>, 1.25; Glucose, 10; CaCl<sub>2</sub>, 2.5; MgCl<sub>2</sub>, 1.5. The slicing buffer was of similar composition as ACSF except (in mM): CaCl<sub>2</sub>, 1; MgCl<sub>2</sub>, 5. The low chloride intracellular pipette (internal) solution for patching neurons in current clamp mode contained (in mM): KCl, 20; KGluconate, 100; HEPES, 10; Mg-ATP: 4; Na-GTP: 0.3; Na-Phosphocreatine, 10, pH 7.4, 295 mOsm. EPSCs were recorded in voltage clamp mode (holding potential -70mV) with the low chloride internal solution. For recording IPSCs in voltage clamp mode (holding potential – 70mV, in the presence of NBQX), a high chloride internal solution was used (in mM): KCl, 120; HEPES, 10; Mg-ATP: 4; Na-GTP: 0.3; Na-Phosphocreatine, 10, pH 7.4, 295 mOsm. Drugs: Acetylcholine chloride (ACh, 1 µM - 10 mM), Atropine sulfate (Atropine, 50 µM), Mecamylamine hydrochloride (Meca, 10 µM), Bicuculline methiodide (BCC, 20 µM) and Tetrodotoxin (TTX, 1 µM) were purchased from Sigma; D-(–)-2-amino-5-phosphonopentanoic acid (D-APV, 50 µM), 2, 3-Dioxo-6-nitro-1,2,3,4-tetrahydrobenzo[f]quinoxaline-7-sulfonamide disodium salt (NBQX, 10 µM), Gabazine (10 µM) and CGP55845 hydrochloride (2 µM) were purchased from Tocris. Drugs were bath applied, except for ACh which was applied by pressure injection with a picospritzer.

### Intracellular recording in slices

Glass pipettes (4 – 7 MΩ) were pulled with a Sutter P1000 puller (Sutter instruments). Layer 2/3 cells were visualized with an Olympus BX61WI microscope coupled with a 40x water immersion lens (Olympus), infrared-DIC optics and CCD camera (Qimaging).



In GAD-67-GFP-SOM-Cre-Arch slices used in Fig. 2i-k, putative VIP neurons were identified by their expression of GFP, their RS characteristic and lack of hyperpolarizing response to green light stimulation. In GAD-67-GFP-SOM-Cre-Arch slices used in Fig. 3c-e, fast-spiking (FS) neurons were identified by their expression of GFP and their FS characteristic. In SOM-Cre-Arch slices in Fig. 3f-h, in GAD-67-GFP slices in Supplementary Figs. 5k-m, in VIP-Cre-Arch slices in Supplementary Fig. 13c-d and in 5HT3aR-Cre-Arch slices in Supplementary Fig. 13g-h, regular-spiking (RS) putative excitatory neurons (PYR) were identified by the absence of GFP as well as their morphological and electrophysiological characteristics: pyramidal-shaped soma, apical dendrites radially projecting towards the pial and basal dendrites directed downwards and laterally<sup>65</sup> and adaptation of spike frequency when stimulated with a constant current<sup>66</sup>. A subset of experiments in Supplementary Figs. 5k-m was performed in C57BL/6 slices where PYR neurons were identified by their distinct morphological and electrophysiological characteristics as described above.

Recordings were performed with a multiclamp 700B amplifier and digidata 1440A data acquisition system, with pClamp software in both the current- and voltage-clamp modes. Optogenetic stimulation of Arch was performed using output from a Lumen 200 fluorescence lamp (5% light output, Prior Scientific, Inc.) through a green filter.

### Slice physiology analysis

Analysis was performed with the Clampfit 10.2.0.12 software. In Figs 2c, 2e, 2h, 2k, 2n, 3b, 3e, 3h, Supplementary Figs 3, 4c, 6b, 7, 8c, 8f, 8i, 13b, 13d, 13f, 13h, 13j, the ACh induced changes in response was defined as  $(\text{ACh response})_{\text{after drug}} - (\text{ACh response})_{\text{before drug}}$  where (ACh response) was computed over 10 s. Supplementary Fig. 6c-e was analyzed using the Mini Analysis Program (Synaptosoft, v 6.0.7): The latency was defined as the time to reach peak amplitude and computed by finding the first data point to the left of the peak that showed 0.5% of the peak amplitude before subtracting the time at this point from the time at the peak. The peak amplitude was calculated by taking the amplitude at the local maximum minus the average baseline. The charge was computed as the area under the curve by taking an integral of amplitude from the first data point to the left of the peak that showed 0.5% of the peak amplitude to the first data point to the right of the peak that showed 0.37 of the peak amplitude.

### Immunohistochemistry

SOM-TD mice (P34, Supplementary Fig. 6f) were anesthetized with 4% isoflurane and perfused transcardially with saline followed by chilled 4% paraformaldehyde in 0.1 M PBS. The brains were then postfixed in 4% paraformaldehyde in 0.1 M PBS (<4°C) overnight. The fixed brains were sectioned into 50 µm visual cortical slices with a vibratome and then blocked in 10% normal goat serum with 1% triton in PBS (1 hour, room temperature) before being stained with rabbit anti-M1 and anti-M2 (1:200, Millipore, AB5164, AB5166) or rabbit anti-nAChR alpha4 and rabbit anti-nAChR beta2 or rabbit anti-nAChR alpha7 (1:200, Abcam, ab41172, ab55980, ab23832)<sup>67</sup> overnight (< 4 °C). This was followed by a 3 hour incubation in Alexa Fluor 488 goat anti-rabbit (1:200, Invitrogen, A11034) before being mounted on a glass slide with the Vectashield Hardset mounting media (Vector Labs). The

slides were imaged using a confocal microscope (Zeiss LSM 5 Pascal Exciter) and the images were analyzed for co-localization of tdTomato positive SOM neurons and the respective cholinergic receptors stains.

### Statistics and general method

Detailed sampling statistics for all figures are provided in Supplementary Tables 1-2. The normality test was performed to check if samples can be described by a Gaussian distribution before the standard t-test was used to compare responses across populations of neurons and across animals. Two-tailed, paired t-test was used for comparisons unless indicated. In a small subset of experiments that did not pass the normality test, non-parametric statistics were used. Error bars indicate SEM unless indicated. Blind experiments were not performed in the study but the same criteria were applied to all allocated groups for comparisons. No randomization was performed for the study. No statistical methods were used to predetermine sample sizes, but our sample sizes are similar to those reported in previous publications<sup>21, 37</sup>.

### Supplementary Material

Refer to Web version on PubMed Central for supplementary material.

### Acknowledgments

We thank Guoping Feng and Holly Robertson for providing ChAT-ChR2 mice; Ed Boyden and Aimei Yang for providing Arch virus; Chuong Le for technical assistance with viral injections and immunohistochemistry; Sami El Boustani, Rafiq Huda and Michael Goard of the Sur Lab for careful reading of manuscript and critical technical advice; Travis Emery for technical assistance with the optogenetics laser setup; and Jitendra Sharma for technical assistance. We especially thank Bernardo Sabatini, Adam Granger, Weifeng Xu and Zhanyan Fu for providing critical technical advice. This work was supported by an A\*STAR (Singapore) Fellowship (NC), and grants from the NIH (R01EY007023, R01EY018648), NSF and the Simons Foundation (MS).

### References

1. Kitt CA, Höhmann C, Coyle JT, Price DL. Cholinergic innervation of mouse forebrain structures. *The Journal of Comparative Neurology*. 1994; 341:117. [PubMed: 8006218]
2. Metherate R, Cox C, Ashe J. Cellular bases of neocortical activation: modulation of neural oscillations by the nucleus basalis and endogenous acetylcholine. *The Journal of Neuroscience*. 1992; 12:4701–4711. [PubMed: 1361197]
3. Goard M, Dan Y. Basal forebrain activation enhances cortical coding of natural scenes. *Nature Neuroscience*. 2009; 12:1444. [PubMed: 19801988]
4. Harris KD, Thiele A. Cortical state and attention. *Nature reviews. Neuroscience*. 2011; 12:509–523. [PubMed: 21829219]
5. Herrero JL, et al. Acetylcholine contributes through muscarinic receptors to attentional modulation in V1. *Nature*. 2008; 454:1110. [PubMed: 18633352]
6. Cohen MR, Maunsell JHR. Attention improves performance primarily by reducing interneuronal correlations. *Nature Neuroscience*. 2009; 12:1594–1600. [PubMed: 19915566]
7. Thiele A. Optimizing brain processing. *Nature neuroscience*. 2009; 12:1359–1360. [PubMed: 19861947]
8. Li, C.-y.T.; Poo, M.-m.; Dan, Y. Burst Spiking of a Single Cortical Neuron Modifies Global Brain State. *Science*. 2009; 324:643–646. [PubMed: 19407203]

9. Gentet LJ, Avermann M, Matyas F, Staiger JF, Petersen CCH. Membrane Potential Dynamics of GABAergic Neurons in the Barrel Cortex of Behaving Mice. *Neuron*. 2010; 65:422–435. [PubMed: 20159454]
10. Renart A, et al. The Asynchronous State in Cortical Circuits. *Science*. 2010; 327:587–590. [PubMed: 20110507]
11. King PD, Zylberberg J, DeWeese MR. Inhibitory Interneurons Decorrelate Excitatory Cells to Drive Sparse Code Formation in a Spiking Model of V1. *The Journal of Neuroscience*. 2013; 33:5475–5485. [PubMed: 23536063]
12. Sippy T, Yuste R. Decorrelating action of inhibition in neocortical networks. *The Journal of Neuroscience*. 2013; 33:9813–9830. [PubMed: 23739978]
13. Klausberger T, et al. Brain-state-and cell-type-specific firing of hippocampal interneurons in vivo. *Nature*. 2003; 421:844–848. [PubMed: 12594513]
14. Cardin JA, et al. Driving fast-spiking cells induces gamma rhythm and controls sensory responses. *Nature*. 2009; 459:663–667. [PubMed: 19396156]
15. Arroyo S, Bennett C, Aziz D, Brown SP, Hestrin S. Prolonged Disynaptic Inhibition in the Cortex Mediated by Slow, Non- $\alpha 7$  Nicotinic Excitation of a Specific Subset of Cortical Interneurons. *The Journal of Neuroscience*. 2012; 32:3859–3864. [PubMed: 22423106]
16. Xiang Z, Huguenard JR, Prince DA. Cholinergic Switching Within Neocortical Inhibitory Networks. *Science*. 1998; 281:985–988. [PubMed: 9703513]
17. Kawaguchi Y. Selective Cholinergic Modulation of Cortical GABAergic Cell Subtypes. *J Neurophysiol*. 1997; 78:1743–1747. [PubMed: 9310461]
18. Fanselow EE, Richardson KA, Connors BW. Selective, State-Dependent Activation of Somatostatin-Expressing Inhibitory Interneurons in Mouse Neocortex. *Journal of Neurophysiology*. 2008; 100:2640–2652. [PubMed: 18799598]
19. Xu H, Jeong H-Y, Tremblay R, Rudy B. Neocortical Somatostatin-Expressing GABAergic Interneurons Disinhibit the Thalamorecipient Layer 4. *Neuron*. 2013; 77:155–167. [PubMed: 23312523]
20. Alitto HJ, Dan Y. Cell-type-specific modulation of neocortical activity by basal forebrain input. *Frontiers in systems neuroscience*. 2012; 6
21. Fu Y, et al. A Cortical Circuit for Gain Control by Behavioral State. *Cell*. 2014; 156:1139–1152. [PubMed: 24630718]
22. Arroyo S, Bennett C, Hestrin S. Nicotinic modulation of cortical circuits. *Frontiers in Neural Circuits*. 2014; 8
23. Letzkus JJ, et al. A disinhibitory microcircuit for associative fear learning in the auditory cortex. *Nature*. 2011; 480:331–335. [PubMed: 22158104]
24. Kalmbach A, Waters J. Modulation of high-and low-frequency components of the cortical local field potential via nicotinic and muscarinic acetylcholine receptors in anesthetized mice. *Journal of Neurophysiology*. 2014; 111:258–272. [PubMed: 24155009]
25. Chen N, et al. Nucleus basalis-enabled stimulus-specific plasticity in the visual cortex is mediated by astrocytes. *Proceedings of the National Academy of Sciences, USA*. 2012
26. Pfeffer CK, Xue M, He M, Huang ZJ, Scanziani M. Inhibition of inhibition in visual cortex: the logic of connections between molecularly distinct interneurons. *Nature neuroscience*. 2013
27. Jiang X, Wang G, Lee AJ, Stornetta RL, Zhu JJ. The organization of two new cortical interneuronal circuits. *Nature neuroscience*. 2013; 16:210–218. [PubMed: 23313910]
28. Pi H-J, et al. Cortical interneurons that specialize in disinhibitory control. *Nature*. 2013; 503:521–524. [PubMed: 24097352]
29. Kruglikov I, Rudy B. Perisomatic GABA release and thalamocortical integration onto neocortical excitatory cells are regulated by neuromodulators. *Neuron*. 2008; 58:911–924. [PubMed: 18579081]
30. Fino E, Yuste R. Dense Inhibitory Connectivity in Neocortex. *Neuron*. 2011; 69:1188–1203. [PubMed: 21435562]

31. Bessie Aramakis V, Bandrowski AE, Ashe JH. Muscarinic reduction of GABAergic synaptic potentials results in disinhibition of the AMPA/kainate-mediated EPSP in auditory cortex. *Brain Res.* 1997; 758:107–117. [PubMed: 9203539]
32. McCormick DA, Prince DA. Mechanisms of action of acetylcholine in the guinea-pig cerebral cortex in vitro. *The Journal of Physiology.* 1986; 375:169–194. [PubMed: 2879035]
33. Giessel AJ, Sabatini BL. M1 Muscarinic Receptors Boost Synaptic Potentials and Calcium Influx in Dendritic Spines by Inhibiting Postsynaptic SK Channels. *Neuron.* 2010; 68:936. [PubMed: 21145006]
34. Buchanan KA, Petrovic MM, Chamberlain SEL, Marrion NV, Mellor JR. Facilitation of Long-Term Potentiation by Muscarinic M1 Receptors Is Mediated by Inhibition of SK Channels. *Neuron.* 2010; 68:948. [PubMed: 21145007]
35. De La Rocha J, Doiron B, Eric Shea-Brown KJ, cacute, Reyes A. Correlation between neural spike trains increases with firing rate. *Nature.* 2007; 448:802–806. [PubMed: 17700699]
36. Rudy B, Fishell G, Lee S, Hjerling-Leffler J. Three groups of interneurons account for nearly 100% of neocortical GABAergic neurons. *Developmental Neurobiology.* 2011; 71:45–61. [PubMed: 21154909]
37. Adesnik H, Bruns W, Taniguchi H, Huang ZJ, Scanziani M. A neural circuit for spatial summation in visual cortex. *Nature.* 2012; 490:226–231. [PubMed: 23060193]
38. Gentet LJ, et al. Unique functional properties of somatostatin-expressing GABAergic neurons in mouse barrel cortex. *Nature neuroscience.* 2012; 15:607–612. [PubMed: 22366760]
39. Marrosu F, et al. Microdialysis measurement of cortical and hippocampal acetylcholine release during sleep-wake cycle in freely moving cats. *Brain Research.* 1995; 671:329–332. [PubMed: 7743225]
40. Poulet JFA, Fernandez LMJ, Crochet S, Petersen CCH. Thalamic control of cortical states. *Nature Neuroscience.* 2012; 15:370–372. [PubMed: 22267163]
41. Harris KD. Top-Down Control of Cortical State. *Neuron.* 2013; 79:408–410. [PubMed: 23931991]
42. Vanderwolf C, Stewart D. Thalamic control of neocortical activation: a critical re-evaluation. *Brain research bulletin.* 1988; 20:529–538. [PubMed: 3395864]
43. Compte A, Sanchez-Vives MV, McCormick DA, Wang X-J. Cellular and network mechanisms of slow oscillatory activity (< 1 Hz) and wave propagations in a cortical network model. *Journal of neurophysiology.* 2003; 89:2707–2725. [PubMed: 12612051]
44. Sakata S, Harris KD. Laminar structure of spontaneous and sensory-evoked population activity in auditory cortex. *Neuron.* 2009; 64:404–418. [PubMed: 19914188]
45. McCormick DA. Neurotransmitter actions in the thalamus and cerebral cortex and their role in neuromodulation of thalamocortical activity. *Progress in Neurobiology.* 1992; 39:337. [PubMed: 1354387]
46. Fries P, Reynolds JH, Rorie AE, Desimone R. Modulation of Oscillatory Neuronal Synchronization by Selective Visual Attention. *Science.* 2001; 291:1560–1563. [PubMed: 11222864]
47. Roberts MJ, et al. Acetylcholine Dynamically Controls Spatial Integration in Marmoset Primary Visual Cortex. *Journal of Neurophysiology.* 2005; 93:2062–2072. [PubMed: 15548624]
48. Vinje WE, Gallant JL. Sparse coding and decorrelation in primary visual cortex during natural vision. *Science.* 2000; 287:1273–1276. [PubMed: 10678835]
49. Gieselmann M, Thiele A. Comparison of spatial integration and surround suppression characteristics in spiking activity and the local field potential in macaque V1. *European Journal of Neuroscience.* 2008; 28:447–459. [PubMed: 18702717]
50. Müller CM, Singer W. Acetylcholine-induced inhibition in the cat visual cortex is mediated by a GABAergic mechanism. *Brain Research.* 1989; 487:335–342. [PubMed: 2731048]
51. Zhao S, et al. Cell type-specific channelrhodopsin-2 transgenic mice for optogenetic dissection of neural circuitry function. *Nature methods.* 2011; 8:745–752. [PubMed: 21985008]
52. Madisen L, et al. A robust and high-throughput Cre reporting and characterization system for the whole mouse brain. *Nature neuroscience.* 2009; 13:133–140. [PubMed: 20023653]

53. Chow BY, et al. High-performance genetically targetable optical neural silencing by light-driven proton pumps. *Nature*. 2010; 463:98–102. [PubMed: 20054397]
54. Wilson NR, Runyan CA, Wang FL, Sur M. Division and subtraction by distinct cortical inhibitory networks in vivo. *Nature*. 2012; 488:343–348. [PubMed: 22878717]
55. Runyan CA, et al. Response Features of Parvalbumin-Expressing Interneurons Suggest Precise Roles for Subtypes of Inhibition in Visual Cortex. *Neuron*. 2010; 67:847–857. [PubMed: 20826315]
56. Kuhlman SJ, Huang ZJ. High-resolution labeling and functional manipulation of specific neuron types in mouse brain by Cre-activated viral gene expression. *PLoS One*. 2008; 3:e2005. [PubMed: 18414675]
57. Tamamaki N, et al. Green fluorescent protein expression and colocalization with calretinin, parvalbumin, and somatostatin in the GAD67-GFP knock-in mouse. *The Journal of Comparative Neurology*. 2003; 467:60–79. [PubMed: 14574680]
58. Pologruto TA, Sabatini BL, Svoboda K. ScanImage: flexible software for operating laser scanning microscopes. *Biomed Eng Online*. 2003; 2:13. [PubMed: 12801419]
59. Joshi S, Hawken MJ. Loose-patch-juxtacellular recording in vivo--A method for functional characterization and labeling of neurons in macaque V1. *Journal of Neuroscience Methods*. 2006; 156:37–49. [PubMed: 16540174]
60. Cardin JA, et al. Targeted optogenetic stimulation and recording of neurons in vivo using cell-type-specific expression of Channelrhodopsin-2. *Nature protocols*. 2010; 5:247–254. [PubMed: 20134425]
61. Brainard DH. The Psychophysics Toolbox. *Spatial Vision*. 1997; 10:433. [PubMed: 9176952]
62. Kalmbach A, Hedrick T, Waters J. Selective optogenetic stimulation of cholinergic axons in neocortex. *Journal of Neurophysiology*. 2012; 107:2008–2019. [PubMed: 22236708]
63. von Engelhardt J, Eliava M, Meyer AH, Rozov A, Monyer H. Functional Characterization of Intrinsic Cholinergic Interneurons in the Cortex. *The Journal of Neuroscience*. 2007; 27:5633–5642. [PubMed: 17522308]
64. Tricoire L, Cea-Del Rio CA. Illuminating Cholinergic Microcircuits in the Neocortex. *The Journal of Neuroscience*. 2007; 27:12119–12120. [PubMed: 17989276]
65. DeFelipe J, Fariñas I. The pyramidal neuron of the cerebral cortex: Morphological and chemical characteristics of the synaptic inputs. *Progress in Neurobiology*. 1992; 39:563–607. [PubMed: 1410442]
66. Connors BW, Gutnick MJ. Intrinsic firing patterns of diverse neocortical neurons. *Trends in Neurosciences*. 1990; 13:99–104. [PubMed: 1691879]
67. Prestori F, et al. Gating of long-term potentiation by nicotinic acetylcholine receptors at the cerebellum input stage. *PloS one*. 2013; 8:e64828. [PubMed: 23741401]

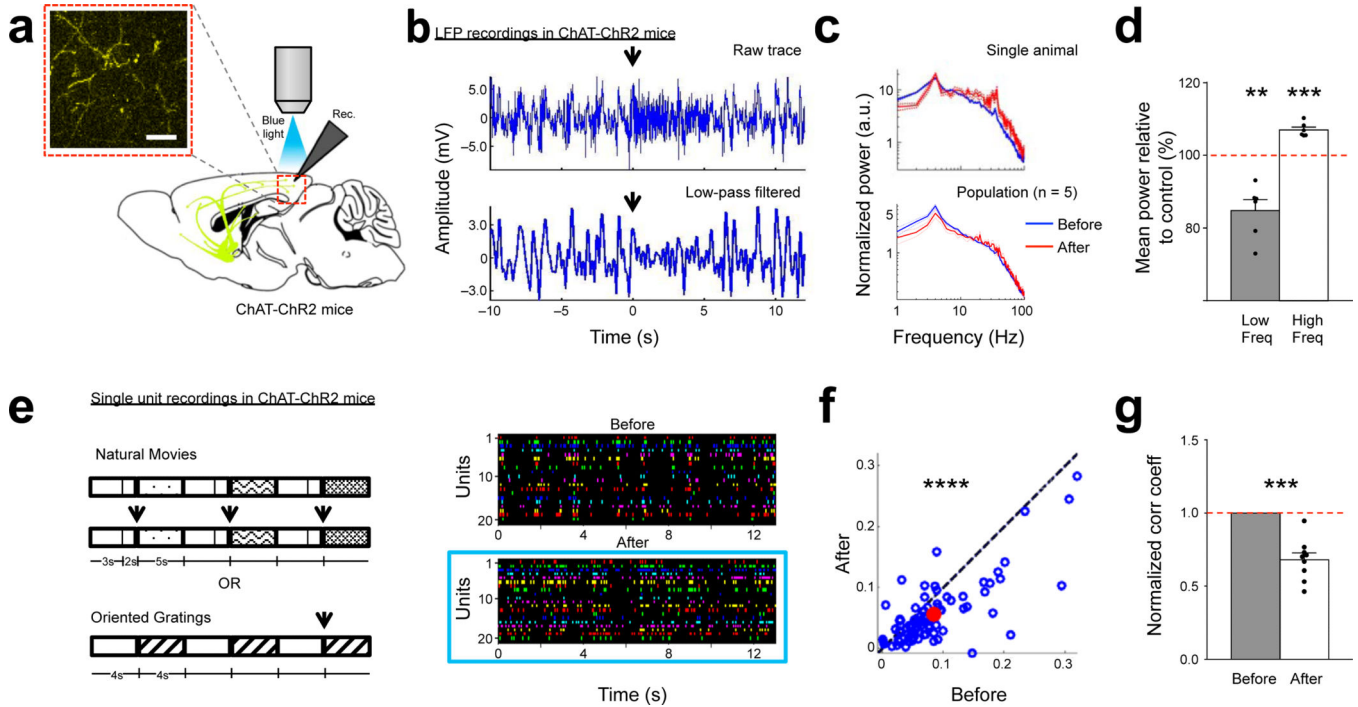


**Figure 1.**

Optogenetic stimulation of ChAT-ChR2 expressing axons induces LFP desynchronization and decorrelation in layer 2/3 V1 neurons. **(a)** Experimental setup for LFP or single unit recording, with ChAT-ChR2 blue light stimulation through the objective (adapted from Paxinos GFK, Franklin KBJ, Academic Press, 2001). **(Inset)** Fluorescence image of ChAT-ChR2 axons in V1. Scale bar, 20  $\mu$ m. **(b)** LFP desynchronization during ChAT-ChR2 stimulation at  $t = 0$  s (arrow). **(Top)** Raw trace. **(Bottom)** Low-pass filtered  $< 5$  Hz. **(c)** **(Top)** Example normalized power spectrum in an animal, 1s before (blue) and after (red) ChAT-ChR2 stimulation, averaged over 10 trials. **(Bottom)** Population mean normalized power spectrum across animals. Dotted lines indicate SEM. **(d)** ChAT-ChR2 stimulation induces a decrease in power of low frequency events ( $<10$  Hz, mean power relative to control  $\pm$  SEM,  $84.8 \pm 2.99$  %,  $p = 0.0039$ , paired t-test,  $n = 5$  animals) and increase in high frequency events (10 – 100 Hz,  $107 \pm 0.776$  %,  $p = 0.0003$ , paired t-test). **(e)** **(Left)** Visual and ChAT-ChR2 stimulation protocol. ‘Natural movies’ comprised 3 movies of 5s duration (patterned boxes). ‘Oriented gratings’ comprised 3 trials of alternating 4s of blank screen and 4s of oriented gratings. ChAT-ChR2 stimulation is indicated by arrows. **(Right)** An example experiment showing neuronal decorrelation before (control, top) and after ChAT-ChR2 stimulation (blue box, bottom). Each panel shows responses of multiple single units recorded simultaneously during presentation of natural movies. Each unit is indicated by a different color. **(f)** Scatter plot showing single unit correlation coefficients before and after ChAT-ChR2 stimulation. Blue circles represent mean Pearson correlation coefficients for each neuron; red circle represents population averaged correlation coefficient.  $n = 85$  units from 9 animals,  $P < 0.0001$ , paired t-test, comparing mean correlation coefficients for each unit before and after photostimulation. **(g)** ChAT-ChR2 stimulation induces a significant decrease in the population averaged normalized correlation coefficient across experiments.  $n = 85$  units from 9 animals,  $P < 0.0001$ , paired t-test, comparing mean correlation coefficients for each unit before and after photostimulation.



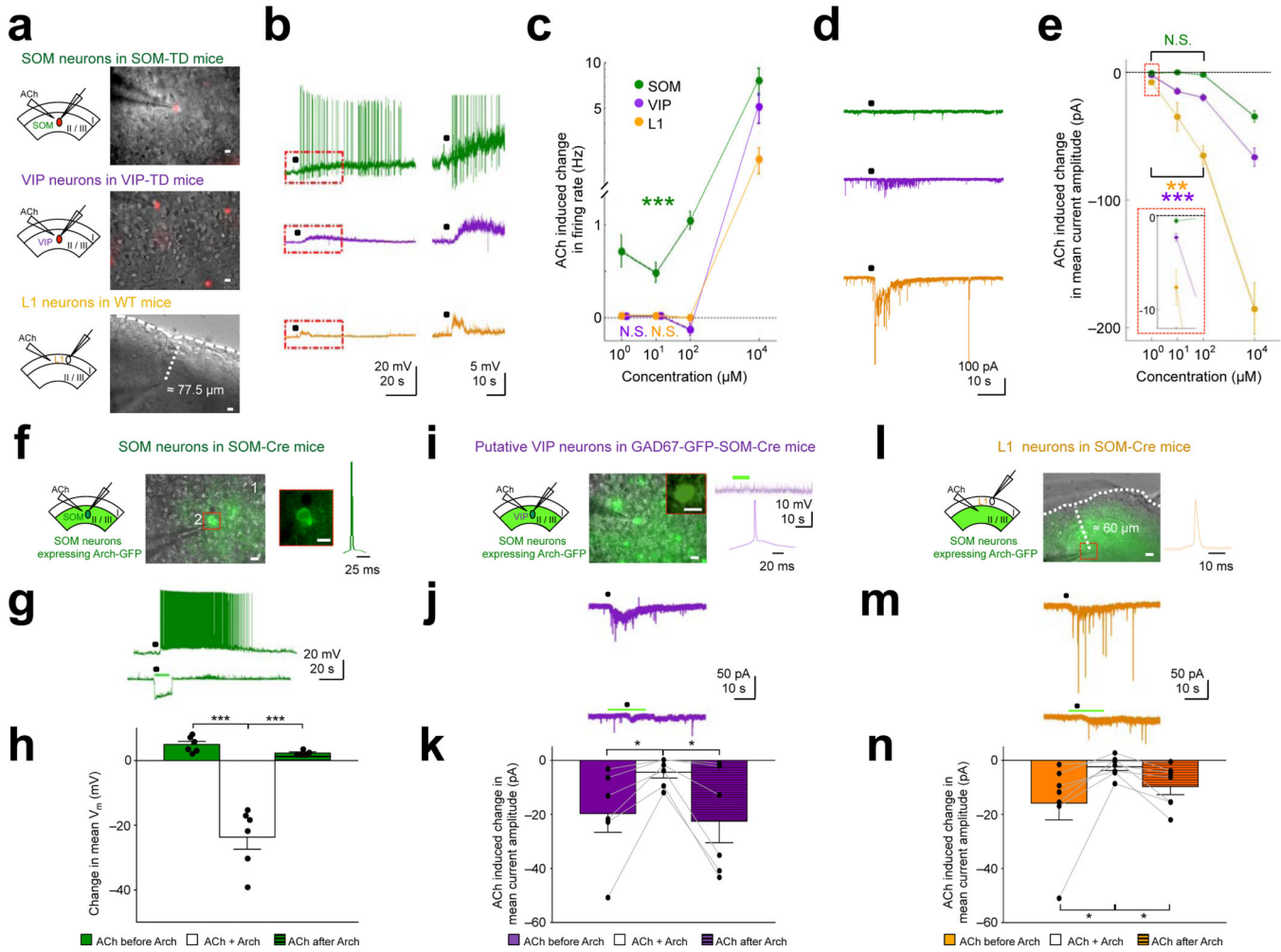
= 9 animals,  $p = 0.0001$ , paired t-test, comparing population averaged correlation coefficients across animals before and after photostimulation. \*\*  $p < 0.01$ , \*\*\*  $p < 0.001$ , \*\*\*\*  $p < 0.0001$ .

Author Manuscript

Author Manuscript

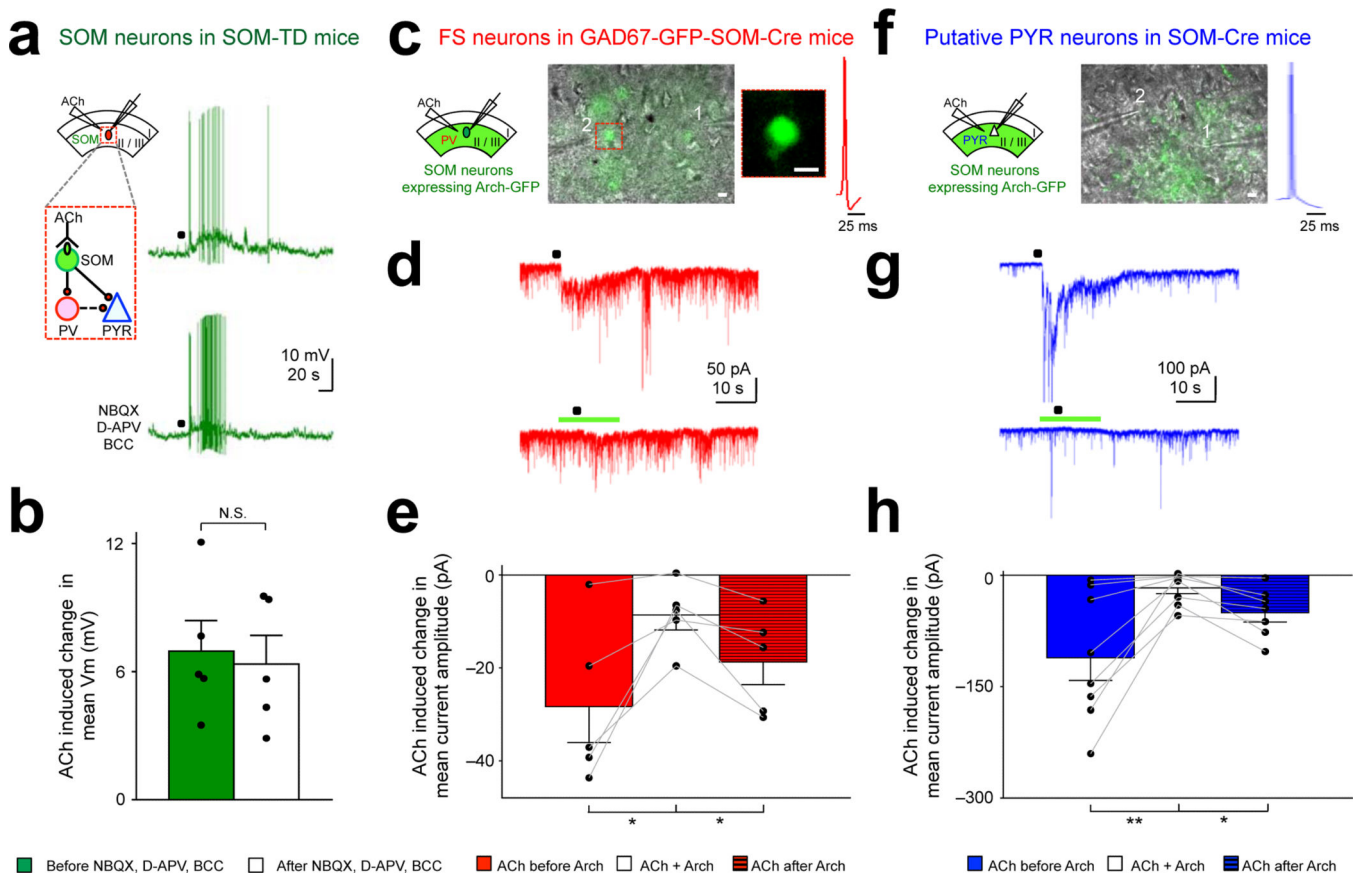
Author Manuscript

Author Manuscript



**Figure 2.** ACh induces facilitation at different dynamic ranges in layer 2/3 SOM, VIP and L1 inhibitory neurons in V1 slices. VIP and L1 neurons also receive inhibitory input from SOM neurons. **(a)** Merged fluorescence and differential interference contrast (DIC) images of **(Top)** a tdTomato positive SOM neuron patched in a SOM-TD slice, **(Middle)** VIP neuron in VIP-TD slice and **(Bottom)** L1 neuron in WT slice. Scale bar, 10  $\mu\text{m}$ . **(Inset)** Configuration of whole-cell patch-clamp recording in slices during ACh application. Figs. 2b-c, 2g-h were performed with low chloride internal solution in current clamp mode. Fig. 2d-e, 2j-k, 2m-n were recorded in voltage clamp mode with high chloride internal solution in NBQX. **(b)** **(Left)** Local ACh application (black dot; 100  $\mu\text{M}$ ) evoked **(Top)** a transient train of action potentials in SOM neurons and **(Middle)** depolarization in VIP and **(Bottom)** L1 neurons. **(Right)** The same traces demarcated by dotted red lines on the left in expanded scales. **(c)** Population mean of ACh-induced changes in firing rate (Hz) of SOM, VIP and L1 neurons against ACh pipette concentrations. Error bars indicate 0.5 SEM. Y-axis is plotted in both linear (0 – 1.25) and log scale (> 1.25). SOM: n = 16 neurons in 16 slices from 7 animals, p = 0.00021; VIP: n = 8 neurons in 7 slices from 4 animals, p = 0.4736; L1: n = 7 neurons in 7 slices from 3 animals, p = 0.1639, paired t-test, comparing firing rate changes evoked by 1–100  $\mu\text{M}$  ACh with null responses. **(d)** **(Top)** Local ACh application (black dot; 100  $\mu\text{M}$ )

evokes smaller NBQX-insensitive inward currents in SOM neurons than in (*Middle*) VIP and (*Bottom*) L1 neurons. (**e**) Similar to (c) except for ACh-induced changes in mean current amplitude (pA). Inset shows responses in an expanded scale. SOM: n = 9 neurons in 9 slices from 3 animals, p = 0.0809, VIP: n = 10 neurons in 10 slices from 4 animals, p = 0.000172, L1: n = 8 neurons in 7 slices from 3 animals, p = 0.00726, paired t-test, comparing responses at 1-100  $\mu$ M ACh with null responses. (**f**) (*Left*) Same as (a) except in layer 2/3 of SOM-Cre slices where AAV-flex-Arch-GFP virus was injected (shaded green). (*Middle*) Merged fluorescence and DIC images of a GFP-positive, Arch-expressing SOM neuron patched in a SOM-Cre slice. Relative positions of ACh pipette (1) and patch pipette (2) were as indicated. (*Inset*) Magnified image of the SOM neuron patched in previous image. Scale bar, 10  $\mu$ m. (*Right*) A typical spike of a SOM neuron. (**g**) Local ACh application (black dot; 10 mM) evoked a transient train of action potentials in an Arch-expressing SOM neuron which was abolished by green light exposure (green bar). (**h**) Population average of mean  $V_m$  of SOM neurons when ACh was applied before, during and after Arch. n = 6 neurons in 6 slices from 3 animals, p = 0.0003, paired t-test, comparing ACh-induced depolarization in SOM neurons before ( $4.96 \pm 1.00$  mV) and after Arch activation ( $-23.6 \pm 3.80$  mV). (**i**) (*Left and Middle*) Similar to (f) where a layer 2/3 putative VIP neuron identified as GFP positive, non-Arch-expressing and regular-spiking in a GAD67-GFP-SOM-Cre slice was recorded. Scale bar, 10  $\mu$ m. Note that the neuron is completely filled with GFP in contrast to the annular membrane-bound Arch-GFP filling observed in (f). Scale bar, 10  $\mu$ m. (*Right top*) The VIP neuron is identified to be non SOM-expressing as it did not hyperpolarize with green light exposure (green bar). (*Right bottom*) A typical spike of a VIP neuron. (**j**) Local ACh application (black dot; 100  $\mu$ M) evoked IPSCs in a putative VIP neuron which were reduced by green light exposure (green bar). (**k**) Population average of ACh-induced changes in mean current amplitude of putative VIP neurons before, during and after Arch. n = 6 neurons in 6 slices from 3 animals, p = 0.0342, paired t-test, comparing ACh-induced current amplitudes before ( $-19.7 \pm 7$  pA) and after Arch ( $-4.40 \pm 2.09$  pA). (**l**) Similar to (f) where a L1 neuron in a SOM-Cre slice was recorded. Scale bar, 10  $\mu$ m. (**m**) Same as (j) but in L1 neuron. (**n**) Same as (k) but with L1 neurons. n = 7 neurons in 7 slices from 4 animals, p = 0.0389, comparing ACh-induced current amplitudes before ( $-15.8 \pm 6.20$  pA) and after Arch ( $-2.34 \pm 1.41$  pA). \* p < 0.05, \*\* p < 0.01, \*\*\* p < 0.001, N.S., not significant. ACh was applied at 200 ms, 20 psi. See Supplementary Fig. 3.

**Figure 3.**

Direct cholinergic facilitation of SOM responses leads to indirect inhibitory responses in FS (putative PV) and PYR neurons. Recordings in Fig. 3a-b were recorded with low chloride internal solution in current clamp mode. Recordings in Fig. 3d-e and Fig. 3g-h were recorded in voltage clamp mode with high chloride internal solution in NBQX. **(a)** Local ACh application (black dot) evokes a transient train of action potentials in SOM neurons (in SOM-TD slices) which persists in the presence of NBQX, D-APV and BCC. **(Inset)** Proposed mechanism of cholinergic action on SOM, PV and PYR neurons. Red circles and green ovals indicate inhibitory synapses and cholinergic receptors respectively. **(b)** Population average of ACh-induced changes in mean  $V_m$  of SOM neurons before and after bath application of glutamatergic/GABAergic antagonists.  $n = 5$  neurons in 5 slices from 3 animals,  $p = 0.565$ , comparing ACh-induced change in mean  $V_m$  before ( $6.96 \pm 1.44$  mV) and after NBQX, D-APV, BCC ( $6.35 \pm 1.34$  mV). **(c)** Similar to Fig. 2i where GFP positive, non-Arch-expressing, FS neurons in a GAD67-GFP-SOM-Cre slice were recorded. Scale bar, 10  $\mu\text{m}$ . **(d)** Local ACh (black dot) evoked IPSCs in a GFP positive, FS neuron which were reduced by green light (green bar). **(e)** Population average of ACh-induced changes in mean current amplitude of GFP positive neurons before, during and after Arch.  $n = 5$  neurons in 5 slices from 3 animals,  $p = 0.0385$ , paired t-test, comparing ACh-induced current amplitudes before ( $-28.3 \pm 7.74$  pA) and after Arch ( $-8.59 \pm 3.23$  pA). **(f)** Similar to Fig. 2f where GFP negative, putative PYR neuron in a SOM-Cre slice was recorded. Scale bar, 10  $\mu\text{m}$ . **(g)** Same as (d) but in a putative PYR neuron. **(h)** Same as (e) but with putative

PYR neurons.  $n = 8$  neurons in 8 slices from 4 animals,  $p = 0.0091$ , comparing ACh-induced current amplitudes before ( $-111.1 \pm 30.6$  pA) and after Arch ( $-17.1 \pm 7.58$  pA). \*  $p < 0.05$ , \*\*  $p < 0.01$ , N.S., not significant. ACh was applied at 10 mM, 200 ms, 20 psi. See Supplementary Fig. 7.

Author Manuscript

Author Manuscript

Author Manuscript

Author Manuscript

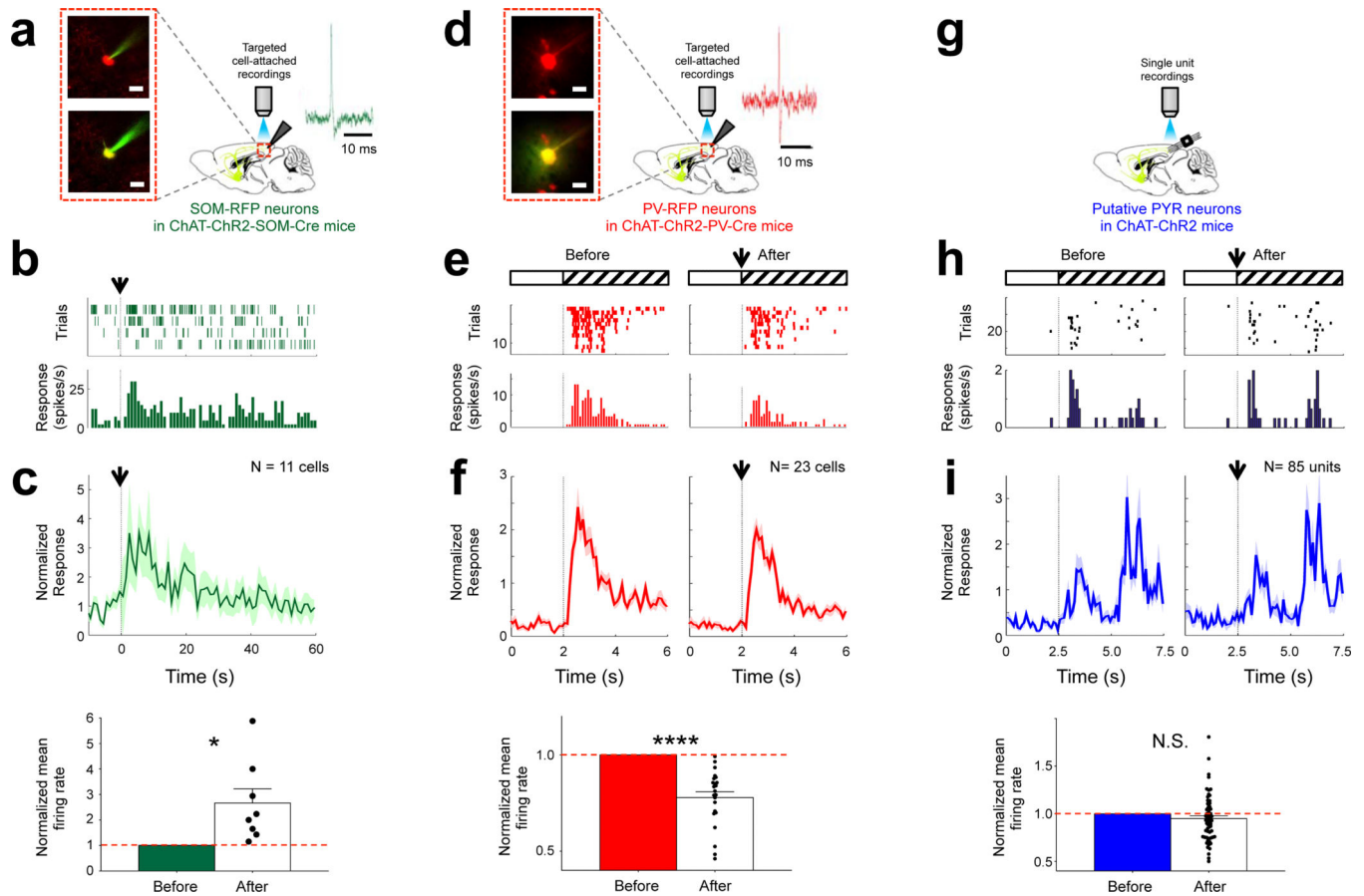


**Figure 4.**

Optogenetic stimulation of ChAT-ChR2 expressing axons evokes diverse responses in V1 layer 2/3 SOM, PV and putative PYR neurons. **(a)** Experimental setup for two-photon guided, cell-attached recording of labeled SOM neurons during ChAT-ChR2 blue light stimulation through objective. *(Left Inset)* RFP positive SOM cells (red) were *(Top)* targeted with a glass pipette containing Alexa 488 dye (green). *(Bottom)* The cell was filled to confirm its identity after recording. Scale bar, 20  $\mu$ m. *(Right Inset)* A typical spike of a SOM neuron in a ChAT-ChR2-SOM-Cre animal. **(b)** *(Top)* Raster plot and *(Bottom)* peristimulus time histogram (PSTH) of responses of a SOM neuron to ChAT-ChR2 stimulation (arrow). **(c)** *(Top)* Normalized PSTH of the responses of SOM neurons to ChAT-ChR2 stimulation (arrow). *(Bottom)* Normalized mean firing rate 8s before and after ChAT-ChR2 stimulation  $n = 11$  neurons from 6 animals,  $p = 0.023$ , paired t-test, comparing normalized firing rate before and after photostimulation; duration of response =  $30.9 \pm 7.49$  s. Baseline firing rate of SOM neurons:  $1.26 \pm 0.531$  Hz. **(d)** Similar to **(a)** where RFP positive PV neurons in ChAT-ChR2-PV Cre mice were recorded. Scale bar, 20  $\mu$ m. **(e)** *(Top)* Raster plot and *(Bottom)* PSTH of visual responses of a PV neuron *(Left)* before and *(Right)* after ChAT-ChR2 stimulation (arrow). ChAT-ChR2 stimulation was synchronized to the start of orientation grating stimuli (patterned bar). A blank grey screen (white bar) preceded visual stimulation. **(f)** *(Top)* Normalized PSTH of the visual responses of PV neurons *(Left)* before and *(Right)* after ChAT-ChR2 stimulation (arrow). *(Bottom)* Normalized mean visual



response (over 4s) before and after ChAT-ChR2 stimulation  $n = 23$  neurons from 4 animals,  $p < 0.0001$ , paired t-test, comparing normalized visual responses before and after photostimulation. Baseline firing rate of PV neurons:  $1.90 \pm 0.542$  Hz. **(g)** Experimental setup for single unit recording in ChAT-ChR2 animals using a tungsten electrode array during ChAT-ChR2 blue light stimulation through the objective. **(h - i)** Similar to Fig. 4e-f except for putative PYR neurons. Random orientation grating or natural movie stimuli were used.  $n = 85$  units from 9 animals,  $p = 0.273$ , paired t-test, comparing normalized visual response before and after photostimulation. Baseline firing rate of PYR neurons:  $0.0865 \pm 0.0242$  Hz. \*  $p < 0.05$ , \*\*\*\*  $p < 0.0001$ . N.S., not significant. Shaded region in Fig. 4c, 4f, 4i indicates SEM.

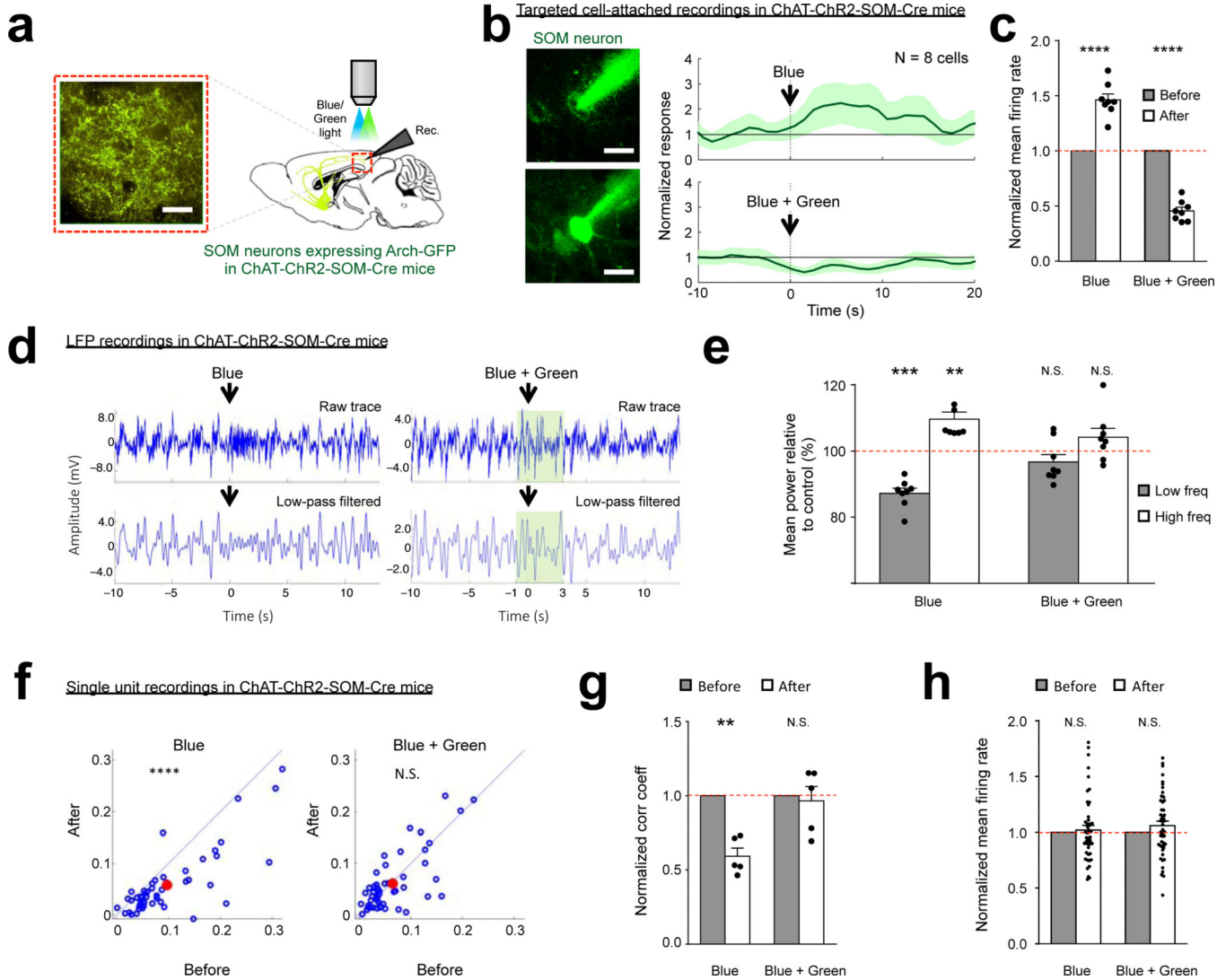


**Figure 5.** ChAT-ChR2 stimulation-induced LFP desynchronization and decorrelation is mediated by SOM neurons. **(a)** Experimental setup for electrophysiological recordings during ChAT-ChR2 blue light stimulation and SOM-Arch green light stimulation through the objective. *(Inset)* Image of Arch-GFP expression in V1. Scale bar, 50  $\mu\text{m}$ . **(b)** *(Left)* *(Top)* An Arch-expressing SOM neuron with membrane-bound GFP was targeted with a glass pipette containing Alexa 488 dye (green). *(Bottom)* The cell was filled to confirm its identity after recording. Scale bar, 10  $\mu\text{m}$ . *(Right)* Normalized mean PSTH of responses of 8 SOM neurons to ChAT-ChR2 stimulation (arrow, 1s duration) *(Top)* without and *(Bottom)* with Arch stimulation (10s duration, preceding ChAT-ChR2 stimulation by 1s). Shaded area indicates SEM. **(c)** ChAT-ChR2 blue light stimulation induced an increase in the normalized mean firing rate measured 8s before and after stimulation ( $p < 0.0001$ ). SOM-Arch green light stimulation reverses this increase ( $p < 0.0001$ ).  $n = 8$  neurons from 4 animals, paired t-test. **(d)** LFP desynchronization during ChAT-ChR2 stimulation at  $t = 0$  s (arrow) *(Left)* was blocked by Arch stimulation (green bar) *(Right)*. *(Top)* Raw trace *(Bottom)* Low-pass filtered. **(e)** Mean power relative to control (%) for low and high frequency bands. **(f)** Single unit recordings before and after stimulation. **(g)** Normalized correlation coefficient before and after stimulation. **(h)** Normalized mean firing rate before and after stimulation.

filtered ( $< 5$  Hz). **(e)** ChAT-ChR2 blue light stimulation induced a decrease in power of low frequency events ( $< 10$  Hz,  $87.3 \pm 1.50$  %,  $p < 0.0001$ ) and increase in high frequency events ( $10 - 100$  Hz,  $109.7 \pm 2.12$  %,  $p = 0.0026$ ) respectively. This was blocked during simultaneous SOM-Arch green light and ChAT-ChR2 blue light stimulation (low frequency:  $96.7 \pm 2.21$  %,  $p = 0.180$ ; high frequency:  $104.2 \pm 2.63$  %,  $p = 0.154$ ).  $n = 8$  animals, comparison with null changes, paired t-test. **(f)** Scatter plot showing the between-cell correlation coefficients (**Left**) before and after ChAT-ChR2 stimulation ( $p < 0.0001$ , paired t-test) and (**Right**) before and after simultaneous SOM-Arch and ChAT-ChR2 stimulation ( $p = 0.432$ ). Each blue circle represents the average correlation coefficient between a single neuron and all other neurons in the same recording; the red circle is the population average.  $n = 49$  units from 5 animals. **(g)** The population averaged normalized correlation coefficient across experiments during ChAT-ChR2 blue light stimulation ( $p = 0.0017$ ) and during simultaneous SOM-Arch green light and ChAT-ChR2 blue light stimulation ( $p = 0.742$ ).  $n = 5$  animals, paired t-test. **(h)** Normalized mean visual response (over 4s) during ChAT-ChR2 blue light stimulation ( $p = 0.630$ ) and during simultaneous ChAT-ChR2 blue light and SOM-Arch green light stimulation ( $p = 0.149$ ).  $n = 49$  units from 5 animals, paired t-test. \*\*  $p < 0.01$ , \*\*\*  $p < 0.001$ , \*\*\*\*  $p < 0.0001$ . N.S., not significant.

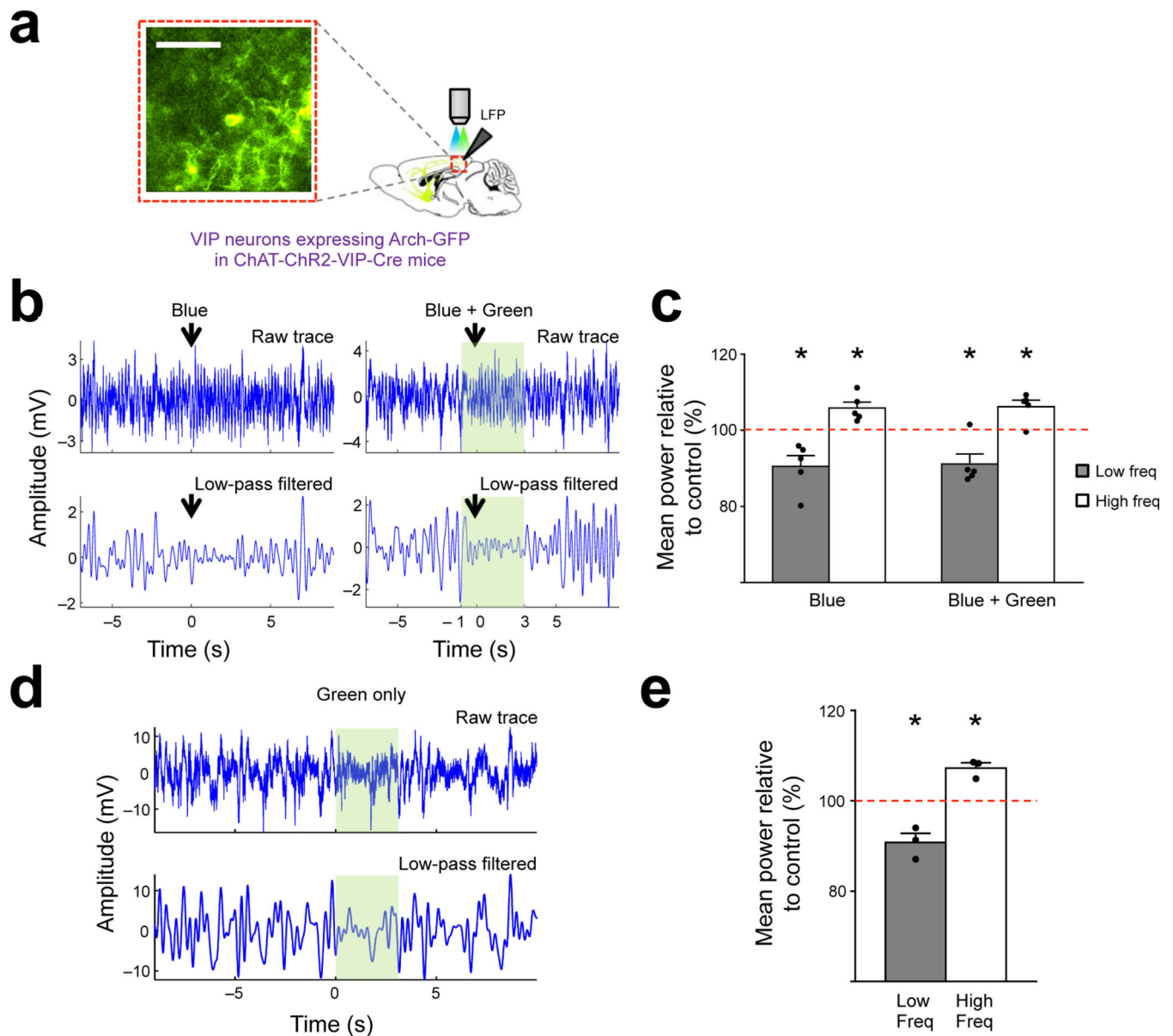


**Figure 6.** VIP neurons do not contribute to ChAT-ChR2 stimulation-induced LFP desynchronization. Hyperpolarization of VIP neurons however can induce desynchronization. **(a)** Experimental setup for LFP recording in ChAT-ChR2-VIP-Cre mice. ChAT-ChR2 blue light stimulation and VIP-Arch green light stimulation were performed through the objective. **(Inset)** Image of Arch-GFP expression in VIP neurons of V1. Scale bar, 50  $\mu$ m. **(b) (Left)** LFP desynchronization during ChAT-ChR2 stimulation at  $t = 0$  s (arrow) was not blocked by **(Right)** Arch stimulation (green bar) of VIP neurons. **(Top)** Raw trace **(Bottom)** Low-pass filtered (<5 Hz). **(c)** The ChAT-ChR2 blue light stimulation induced changes in power of low frequency (<10 Hz,  $90.5 \pm 2.83\%$ ,  $p = 0.0285$ ) and high frequency events (10 – 100 Hz,  $105.8 \pm 1.58\%$ ,  $p = 0.0209$ ) were not blocked during simultaneous VIP-Arch green light and ChAT-ChR2 blue light stimulation (Low frequency:  $91.1 \pm 2.64\%$ ,  $p = 0.0281$ ; High

frequency:  $106.2 \pm 1.70$  %,  $p = 0.0221$ ).  $n = 5$  animals, paired t-test. **(d)** LFP desynchronization during optogenetic Arch stimulation of VIP neurons (green bar). **(Top)** Raw trace. **(Bottom)** Low-pass filtered ( $<5$  Hz). **(e)** Green light stimulation of Arch-expressing VIP neurons induces a significant decrease in power of low frequency events ( $<10$  Hz,  $90.8 \pm 2.02$  %,  $p = 0.0448$ ) and increase in high frequency events (10 – 100 Hz,  $107.2 \pm 1.17$  %,  $p = 0.0254$ ) in ChAT-ChR2-VIP-Cre mice.  $n = 3$  animals, paired t-test. \*  $p < 0.05$ .

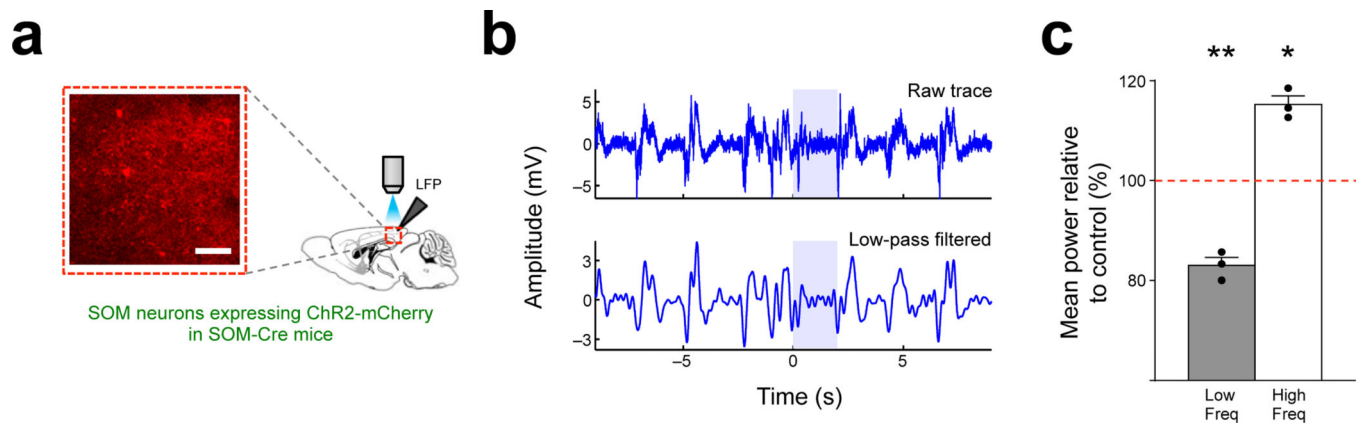


**Figure 7.** Direct ChR2 stimulation of SOM neurons is sufficient to induce LFP desynchronization. **(a)** Experimental setup for LFP recording in SOM-Cre mice during SOM-ChR2 blue light stimulation through the objective. **(Inset)** Image of ChR2-mCherry expression in SOM neurons of V1. Scale bar, 50  $\mu\text{m}$ . **(b)** LFP desynchronization during SOM-ChR2 stimulation (blue bar). **(Top)** Raw trace **(Bottom)** Low-pass filtered (<5 Hz). **(c)** SOM-ChR2 stimulation induces a decrease in power of low frequency events ( $81.7 \pm 1.80\%$ ,  $p = 0.0095$ ) and increase in high frequency events ( $116.8 \pm 1.85\%$ ,  $p = 0.0120$ ).  $n = 3$  animals, paired t-test. \*  $p < 0.05$ , \*\*  $p < 0.01$ .